Engineering Structures 254 (2022) 113478

Contents lists available at ScienceDirect

Engineering Structures

journal homepage: www.elsevier.com/locate/engstruct

Physics-based estimates of drag coefficients for the impact pressure calculation of dense snow avalanches

M.L. Kyburz [a,b,*], B. Sovilla [a], J. Gaume [a,c], C. Ancey [b]

[a] WSL Institute for Snow and Avalanche Research SLF, Davos, Switzerland
[b] Environmental Hydraulics Laboratory, École Polytechnique Fédérale de Lausanne, Lausanne, Switzerland
[c] Snow and Avalanche Simulation Laboratory SLAB, École Polytechnique Fédérale de Lausanne, Lausanne, Switzerland

ARTICLE INFO

Dataset link: https://doi.org/10.5281/zenodo.4394455

Keywords:
Avalanche engineering
Avalanche impact pressure
Granular snow avalanche
Structural design in avalanche-prone terrain

ABSTRACT

In avalanche engineering and hazard mapping, computing impact pressures exerted by avalanches on rigid structures has long been a difficult task that requires combining empirical equations, rules of thumb, engineering judgment and experience. Until the 1990s, well-documented avalanches were seldom, and the main source of information included back-analysis of damage to structures and scarce field measurements. By the 1990s, several field sites were equipped across Europe, and since then they have provided new insights into the physics of impact. The main problem has been the difficulty in interpreting and generalizing the results to propose sound methods for estimating impact pressure. Testing a wide range of flow conditions has also been difficult in the field. To go a step forward in the elaboration of new guidelines for computing avalanche forces, we developed a numerical code based on the Discrete Element Method (DEM), which made it possible to simulate how an avalanche interacts with a rigid obstacle and to study how impact pressure depends on obstacle shape and size, as well as the avalanche flow regime. We extracted pressure and velocity data from the Vallée de la Sionne database to validate the DEM code, calibrate the model parameters, and elaborate avalanche scenarios. We studied four avalanches scenarios related to distinct flow regimes of the avalanche's dense core. In these scenarios, snow cohesion and velocity were imposed at the upstream boundary of the computational domain. Building on earlier work, we generalized an empirical equation for computing impact pressure as a function of snow cohesion, velocity, flow regime, and structure shape and size. Various coefficients were defined and calibrated from our DEM data. Within the range of tested values, we found good agreement between estimated pressure and field data.

1. Introduction

Mountainous areas face various hazards involving the rapid mass movement of a finite volume of material. Typical examples include snow avalanches, debris flows, and rock avalanches. Building structures in this environment involves ensuring that they are placed in a safe area or, if this is not the case, reinforcing them. To that end, computational methods have been developed for estimating runout distances and forces exerted by the flowing mass on fixed obstacles [11–14].

Faced with the thorny problem of estimating impact pressures exerted by complex natural materials, engineers have used analogies between avalanches and related issues in hydrodynamics or geotechnical engineering. Today, a routinely used definition of avalanche impact pressure is copied from the definition of drag force in fluid dynamics when computing the force exerted by a Newtonian fluid on an immersed body [e.g., Chap. 1 in15]:

$$p_x = \frac{F_D}{A} = C_D \frac{\rho}{2} v^2 \tag{1}$$

where F_D is the drag force on the obstacle, A is the projected area facing upstream, C_D is the drag coefficient, ρ is the snow density, and v is the flow velocity [12,16–19]. The main difficulty of the problem lies in the determination of the drag coefficient C_D if we assume that we can determine or measure avalanche velocity and density independently. This problem has long seen only partial answers, owing to the scarcity of relevant avalanche data and the complexity of the avalanche behavior.

1.1. A preliminary note on flow regime

Avalanches involve a wide variety of flow features depending on snow, weather and topography, which in turn generate a diversity of flow behavior [20,21]. Since the earliest developments in avalanche science [22–25], there has been tension between providing a comprehensive classification of avalanches and outlining the overall flow

* Correspondence to: WSL Institute for Snow and Avalanche Research SLF, Flüelastrasse 11, CH 7260, Davos Dorf, Switzerland.
E-mail address: kyburz@slf.ch (M.L. Kyburz).

https://doi.org/10.1016/j.engstruct.2021.113478
Received 19 March 2021; Received in revised form 9 August 2021; Accepted 23 October 2021
Available online 13 January 2022

Nomenclature

A	Obstacle's projected area facing the flow direction
Bo	Bond number
c	Empirical gliding factor [1,2], see Appendix D in [3]
C	Coefficient for C_D in the phenomenological model of Faug [4]
c_1, c_2, c_3	Fitting parameters for f_{coh}
C_{d0}	Empirical coefficient for C_D [5,6]
C_D	Drag coefficient
C_{geo}	Geometry-dependent coefficient of C_D
C_o	Shape-dependent coefficient of C_{geo}
C_r	Flow-regime-dependent coefficient of C_D
C_w	Width-dependent coefficient of C_{geo}
d	Diameter of cylindrical obstacle in Haefeli [1,2]
d_n	Width increment of the obstacle cross section
E	DEM particle Young's modulus
f	Empirical coefficient for C_D from [5,6]
f_{coh}	Impact pressure increase factor due to cohesion
F_D	Drag force on obstacle
Fr	Froude number
g	Gravitational acceleration
h	Avalanche flow height
K	"Pure earth coefficient" from [4,7]
n	Empirical exponent for weighting Fr in [8]
p	Impact pressure
p_x	Impact pressure projected on the plane normal to the streamwise direction
$p_{x,calc}$	Calculated impact pressure of a cohesionless avalanche flow
$p^*_{x,calc}$	Calculated impact pressure of a cohesive avalanche flow
$q_{Bo,Fr}$	Bond to Froude number ratio $q_{Bo,Fr} = Bo/Fr$
R	Curvature radius of ground contour
r_p	DEM particle radius
v	Avalanche flow velocity
v_u	Impact velocity
w	Obstacle width
x	Streamwise direction in DEM
y	Transverse direction to the flow in DEM
z	Vertical direction in DEM
z_R	Vertical position of the resulting force on an obstacle
α	Wedge apex half-angle
β	Incidence angle
ζ	Empirical coefficient for the gravitational pressure contribution [9]
η_F	Efficiency factor [10]
θ	Ground slope
θ_n	Angle between impact surface increment and transverse direction to the flow
κ	Active/passive earth coefficient
μ	DEM Coulomb friction coefficient
ρ	Snow bulk density
ρ_b	DEM bulk density
ρ_m	Snow bulk density upon impact
ρ_p	DEM particle density
$\sigma_{coh} = \sigma_c = \tau_c$	DEM cohesive bond tensile and shear strength

behavior. In engineering, it has been common to distinguish between *flow avalanches* (dense flows of snow, which follows the ground's contours closely) and *powder avalanches* (dilute clouds of snow particles maintained in suspension by air turbulence and moving at a velocity higher than 50 m/s) [26].

Here we are concerned with flow avalanches. Let us provide key characteristics, which will assist us later in quantifying the physical processes at hand: the flow depth h generally does not exceed a few meters, and its mean velocity v ranges from 5 to 25 m/s, although velocities as high as 50 m/s have been observed. On average, the density of snow mobilized by flow avalanches ranges from 150 to 500 kg/m^3. Dry snow tends to be light, whereas wet snow has the highest density. Flow avalanches exhibit varied flow regimes depending on snow consistency (cohesion, moisture and density), velocity and topography. A simple dichotomy used in engineering distinguishes between the inertia- and gravity-dominated regimes (or more concisely, inertial and gravitational regimes). Inertia-dominated avalanches reach high velocities ($v > 10$ m/s) and may overrun low-terrain obstacles. Because of their high velocities, they often entrain ambient air during their descent, and thus a density stratification exists across their flow depth: a dilute layer covers a dense core. Gravity-driven avalanches have low velocities ($v \leq 10$ m/s) and closely follow ground contours. They take the appearance of a granular or viscous flow.

Flow regime and snow consistency are often correlated: cold dry snow tends to form inertial avalanches, whereas wet cohesive snow is more prone to forming gravitational flows. Recent field and laboratory observations have suggested that snow temperature is the key parameter that controls snow cohesion and bulk friction, and thereby the flow dynamics [27–30]: when snow temperature in the flow is lower than −1 °C the regime is dominated by inertial effects, whereas gravitational effects dominate at temperatures higher than this threshold. To highlight the influence of snow temperature, we speak of *cold* or *warm* snow avalanches. Snow texture changes radically as a function of snow temperature and moisture. Dry snow takes the form of a cohesionless powder or, more relevant for this article, a dense granular material composed of small particles, whereas wet snow can take the form of pasty material (like mud) or granular matter with increased particle size [e.g.,28]. This wealth of texture has marked consequences on bulk behavior, and we have taken this point into account in our study.

1.2. Computing impact pressure: a brief state of the art

For a body immersed in a Newtonian fluid, the drag coefficient C_D in Eq. (1) is usually entirely determined by the body's Reynolds number [15]. For non-Newtonian fluids, the mere existence of the drag coefficient is not ensured, and in many cases little is known about its dependence on flow variables or dimensionless numbers. For snow (as a flowing material), the approach has long been speculative and based on sparse observations and measurements. Avalanche forces started to be measured as early as the 1930s in the former Soviet Union [31–33] and from the 1950s on in Western countries. At that time and in the subsequent decades until the 1990s, the measurement techniques were rudimentary. The earliest avalanche-dynamics models were also crude [23,34]; among other things, they were unable to relate avalanche force to flow variables. Just after the devastating winters that struck the Alps in 1951 and 1954, the Swiss structural engineer Adolf Voellmy was commissioned to quantify avalanche forces. Based on field observations of damage to constructions, he published a series of four

papers, in which he set out the first complete theory for computing avalanche velocities and forces depending on the flow regime [35–38]. He ended up with a pressure distribution in the form:

$$p = \rho_m \left(gh + C_D \frac{1}{2} v^2 \right), \tag{2}$$

where ρ_m denotes the snow bulk density upon impact, g is the gravitation acceleration, h is the avalanche flow depth, v its velocity, and $C_D = 1 - (v_u/v)^2(1 - \sin\beta)$ is the drag coefficient, v_u is the impact velocity, and β is the angle of incidence between the flow direction and impacted surface. The impact pressure involves two contributions: a hydrostatic-like contribution $\rho_m g h$, and Bernoulli-like contribution $\frac{1}{2}\rho_m v^2$ weighted by the drag coefficient C_D. A decade later, considering that snow behaves as a cohesionless granular material, whose critical states can be described using Rankine's theory, Salm [39] obtained this expression for the mean flow pressure far from any obstacle

$$p = \kappa \rho \left(gh\cos\theta + \frac{h}{R} v^2 \right) \tag{3}$$

where ρ denotes snow density, R is the ground's radius of curvature, θ is the ground slope, and κ is the active/passive earth coefficient. In that case, the quadratic term in the pressure reflects centrifugal effects. Comparing Eqs. (2) and (3) shows that, for a flow past an obstacle, the pressure distribution is altered due to snow compaction and momentum transfer from the flow to the obstacle.

For subsequent developments, it is instructive to rearrange Eq. (2) by using the Froude number $Fr = v/\sqrt{gh}$:

$$p = C_D \frac{\rho_m}{2} v^2 \left(1 + \frac{2}{C_D} \frac{1}{Fr^2} \right) \tag{4}$$

In analogy to hydraulics, where the Froude number is used to distinguish between supercritical ($Fr > 1$) and subcritical ($Fr < 1$) flows, authors have suggested that this number can also be used to partition the avalanche flow regimes [3,37,39–42]: the inertia-dominated regime – initially called shooting flow (*schiessender Abfluss*) by Voellmy [37] – refers to fast-moving avalanches, while the gravity-dominated regime – also called streaming flow (*strömender Abfluss* – refers to slow-moving avalanches. Whereas in hydraulics there is a neat separation between supercritical and subcritical flows at $Fr = 1$, the situation is less clear for avalanches. Salm [39] suggested that the transition between the inertia- and gravity-dominated regimes occurs at a Froude number $Fr = \sqrt{\kappa\cos\beta}$. Other authors have assumed that the critical Froude number is unity.

For many scientists and practitioners, fast-moving avalanches were long perceived as the most dangerous ones, and this is why emphasis was mainly placed on this flow regime in developing guidelines for computing avalanche features [17–19,43,44]. For high-speed flow avalanches, we typically have $v = O(10 - 30)$ m/s and $h = O(1 - 5)$ m, which leads to Froude numbers in the 1.5–10 range. Authors have thus considered that the Bernoulli-like contribution in Eq. (2) is dominant. Field data have led to drag coefficients in the 1–10 range [5,17,43,45,46]. On rarer occasions, guidelines provide empirical equations for computing avalanche pressure depending on flow regime [3,47]. Since the studies undertaken by Haefeli [10] on snow plasticity, it has been observed that the snow pressure on an obstacle depends on the obstacle's size, a feature not predicted by Eq. (2) or Eq. (3). For creeping snow on a cylindrical obstacle of diameter d, Haefeli [1,2] found that the hydrostatic-like pressure should be weighted by an empirical factor he called the efficiency factor $\eta_F = 1 + ch/d$, with $c \sim 0.6$ (see Appendix D in [3]). The extension of Haefeli's theory to flow avalanches has long been debated.

With the equipment at several field sites across Europe [48], high-accuracy pressure data have been acquired and have shed new light on how avalanche impact pressure is related to the flow variables v and h. From the Col du Lautaret Pass (France) data, Thibert et al. [8] deduced that the drag coefficient varied as a power law of the Froude number:

$$C_D = 2(1 - \cos\alpha) A Fr^{-n} \tag{5}$$

for a wedge-shaped obstacle whose apex angle is 2α, $A = 10.8$ and $n = 1.3$. Later, Thibert et al. [7] used the analogy between snow avalanches and granular flows to propose an extended version

$$C_D = C + K Fr^{-2} \tag{6}$$

where C and K are functions of the obstacle geometry, as well as avalanche flow depth and material properties that were calibrated from laboratory experiments [4]. Analyzing data from the Ryggfonn site (Norway), Gauer et al. [49] suggested that the drag coefficient could be written as

$$C_D = C_{d0} + \frac{f}{Fr^2} \tag{7}$$

where C_{d0} is a constant and $f \approx 4.8\sqrt{h/d}$ [5,6]. At the Vallée de la Sionne field site (Switzerland), Sovilla et al. [50] observed that the assumption of a constant drag coefficient was not realistic, especially for subcritical avalanches for which the drag coefficient varies as $C_D \propto Fr^{-n}$ and thus becomes much larger than unity when $Fr \to 0$. Sovilla et al. [9] observed a linear pressure distribution across the flow depth $p = \zeta\rho g(h - z)$, where z is the height relative to the ground and ζ is a fitted coefficient in the 7.2–8.1 range, but further measurements showed a strong dependence of ζ on the obstacle size and snow consistency [51,52].

In an earlier paper [53], we studied how cohesive avalanches interacted with the instrumented pylon in Vallée de la Sionne. To that end, we used the numerical code described in Section 2.1. We found that the impact pressure on the pylon could be broken down into three contributions:

- The inertial contribution, which is proportional to the velocity squared. This contribution is predominant for fast avalanches in the inertial regime. The $p \propto \rho v^2$ scaling confirms that a Bernoulli approximation can be used to estimate this term.
- The frictional contribution, which originates from force chains between the particles of the granular avalanche [54]. This contribution is dominant in the gravitational regime.
- The cohesive contribution, which originates from the tensile and shear strengths related to the connection between neighboring particles.

The frictional and cohesive impact pressure contributions can be quantitatively linked to the jamming of the particles in the flow's domain of influence (called the "mobilized domain" by a number of authors) in the vicinity of the obstacle [55,56].

We also found that the impact pressure exerted by a cohesive flow can be determined from a factor reflecting the relative importance of cohesive and inertial forces and the impact pressure of a cohesionless flow (see Section 6.2).

1.3. Scientific problem and study objectives

In recent decades, growing evidence has accumulated indicating that Voellmy's physical intuition was correct. Field measurements have confirmed that when an avalanche impacts a rigid structure, it exerts a force that can be decomposed into hydrostatic-like and Bernoulli-like contributions, as shown by Voellmy's Eq. (4). Although this overall pattern seems robust, there is no consensus on the C_D values in Eq. (4), and more specifically the dependence of the drag coefficient C_D on flow regime, snow consistency, and obstacle size and shape.

Filling this knowledge gap would be difficult if we only used field data and laboratory experiments on similar materials, but bridging this gap is now possible using numerical codes based on the Discrete Element Method (DEM). This approach has been applied, for instance, in studying impact forces exerted by granular flows on rigid barriers on the laboratory scale [57–59]. The originality here is that we used real-world avalanches (data recorded in Vallée de la Sionne) to calibrate the model parameters and elaborate avalanche scenarios for

our simulations. Once calibrated, the DEM code was applied to flows past obstacles of varied size and shape for four distinct avalanche scenarios that were typical of the flow regimes outlined in Section 1.1. Based on our results and earlier work, we propose a physics-based practical method for estimating the drag coefficient C_D depending on flow regime and obstacle geometry. The method was tested using data from Vallée de la Sionne.

2. Simulation of avalanche impact pressure on obstacles with DEM

2.1. Avalanche modeling setup and parameters

Flow avalanches have often been considered to behave like dry granular flows [13,60,61], and this analogy has thus been used to model them on the laboratory scale or numerically. In this study, we applied the Discrete Element Method (DEM) to simulate avalanches moving past rigid obstacles using the PFC software from Itasca (Minneapolis, MN, USA). This software is based on the soft-contact algorithm [62,63] to model the interaction between cohesive particles. In this numerical framework, no fluid–solid coupling is considered, and thus the bulk dynamics is entirely ruled by particle contact. This means that in our study we simulated only the avalanche's dense flow part, assuming that the interaction between the solid phase and the interstitial air is negligibly small.

To simulate how avalanches interact with fixed obstacles, we used the numerical setup implemented in an earlier study [56] (see also Supplementary Material S.1 of this article). This setup extended the procedure in our first paper on this topic [53] and made it possible to study obstacles wider than 0.6 m, which corresponds to the Vallée de la Sionne's pylon considered initially (Section 2.2.1). In [53], we showed that our numerical code could reproduce impact pressure measurements on the pylon.

In order to minimize the computational cost of simulations, we considered an isolated volume of granular material flowing past the obstacle. The flowing granular material mimicked a snow avalanche in an area of 11–22×28 m^2 around the obstacle (the exact size depended on the obstacle width). The particle flux was imposed at the up- and downstream boundary. We chose the boundary velocity such that it matched the vertical velocity profile of the selected avalanche scenario. In our numerical setup, the x, y and z directions corresponded to the streamwise, transverse and vertical directions, respectively.

Estimating the material properties of snow mobilized by avalanches is challenging because most studies on the mechanical properties of snow are related to snow samples from an undisturbed snowpack [e.g.,64,65], and from small-scale chute experiments [e.g.,66,67]. However, to the best of our knowledge, the mechanical properties of snow inside avalanches, where snow may experience large shear rates and thermo-mechanical transformations [28,68], is not available. This lack of information led us to use available data on undisturbed snow. For this reason, our study's model parameters must be considered with caution: they are plausible values, not measured ones.

In this paper, we use the material properties and contact law parameters used in our first paper [53].

In our simulations we do not resolve individual snow flakes or ice crystals as DEM particles, as this would result in prohibitive simulation times. Hence, the DEM particles correspond to aggregated snow particles with a particle radius r_p in the range of 32 mm $\leq r_p \leq$ 48 mm, which corresponds to a polydispersity of 20 %. Therefore, the physical properties of the DEM particles also correspond to properties of aggregated snow granules.

We define the density of the spherical DEM particles as ρ_p = 500 kg/m^3. This results in a mean bulk density ρ_b of the undisturbed flowing material, which ranges from 338 kg/m^3 to 379 kg/m^3 and thus agrees well with density values found in field and experimental studies [28,69–71].

It is important to note, that we simulate soft particles, which may exhibit substantial overlap if subject to compressive load to mimick snow compression. The compressibility of snow is well documented in the literature [e.g.,36,72–74]. Hence, we use a particles' Young's modulus of $E = 10^5$ Pa in all simulations, which is in the range of reported values from the literature [e.g.,64,65,75].

We mimick the cohesive material behavior of snow using a cohesive bond contact law. In this contact law a cohesive bond is formed between particles whenever they come in contact. The cohesive bond breaks if the tensile or shear force between the particles exceeds the bond's tensile strength σ_c or shear strength τ_c. Hence, we use the cohesive bond strength $\sigma_{coh} = \sigma_c = \tau_c$ at the particle scale as a measure for cohesion throughout the paper.

Table 1 is a list of the most important material parameters used. Further information on how the contact forces were modeled and our code can be found in the Supplementary Material S.2 of this article and in our earlier studies [53,56].

Table 1
Material properties for the Discrete Element Method (DEM) simulations.

Parameter	Symbol	Value/Range
Particle radius	r_p	40 ± 8 mm
Particle density	ρ_p	500 kg/m^3
Bulk density[a]	ρ_b	338–379 kg/m^3
Young's modulus	E	10^5 Pa
Friction coefficient	μ	0.5

[a] ρ_b results from ρ_p and interstitial voids between the particles and is not a controllable input parameter.

2.2. Obstacle geometries

2.2.1. Vallée de la Sionne measurement obstacles in DEM

In this study, we used measurements collected at the Vallée de la Sionne site to test whether our DEM model was able to reproduce impact pressure measurements on obstacles and sensors of different sizes and geometries. In Vallée de la Sionne, the test site's release area covers 30 ha, and it feeds two main corridors that converge just upstream of the zone where the obstacles and sensors are located (near 1700 m a.s.l.) [76]. Since the late 1990s, more than 70 avalanches (involving artificial and natural releases) have reached the obstacles and have been recorded. Fig. 1 shows side views of the three obstacles in Vallée de la Sionne and the positions of the pressure sensors. These obstacles include a steel pylon of rectangular cross-section, a small concrete wall and a narrow steel wedge [9,77]. We implemented these geometries in our DEM to simulate avalanche pressure on the Vallée de la Sionne obstacles.

The pylon is a 20 m tall steel cantilever with an elongated cross-section in the flow direction of 1.6 × 0.6 m^2. It is equipped with 6 cylindrical pressure sensors with a vertical spacing of 1 m from 0.5 m to 5.5 m above the ground. The cylindrical sensors have a diameter of 0.1 m and protrude upstream into the flow. The avalanche flow velocity is measured at the pylon using 46 optoelectronic sensor pairs vertically distributed from 0.25 m up to 6.0 m above the ground [78]. In the DEM simulations, we reproduced the exact cross-section of the pylon but chose a smaller vertical spacing of 0.26 m instead of the 1 m between the pressure sensors on the real measurement pylon in Vallée de la Sionne to enhance the resolution of the vertical pressure profile. The spacing of 0.26 m corresponded to the vertical location of every second velocity sensor on the pylon.

The second obstacle is a narrow wedge with a flat beam mounted at the leading edge with a frontal width of 0.24 m and a height of 4.5 m. The beam accommodates four cylindrical pressure sensors with a diameter of 0.25 m, which protrude upstream into the flow. The sensors are located 1.3 m, 2.3 m, 3.3 m and 4.3 m above the ground. The sidewall of the wedge is at an opening angle of 5° from the symmetry axis of the obstacle in the flow direction. Instead of the flat

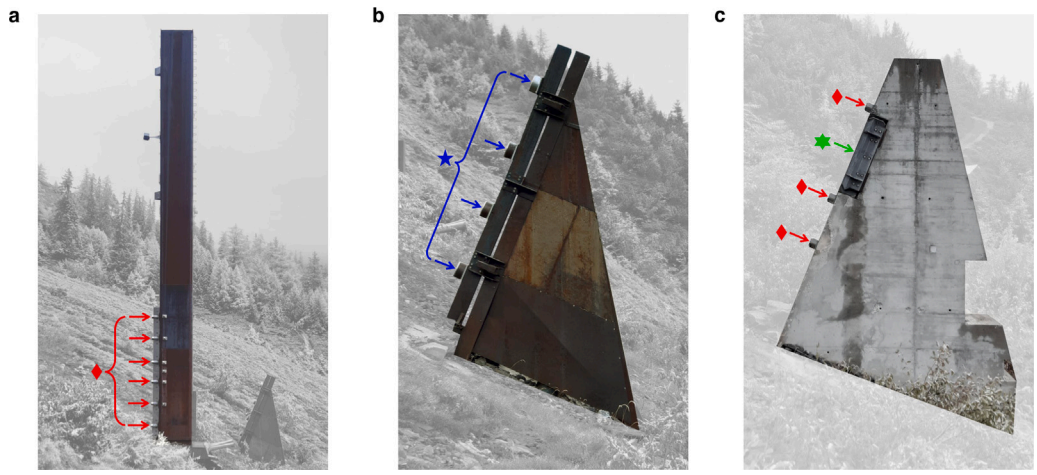

Fig. 1. Vallée de la Sionne measurement obstacles. Panels a, b and c show side views of the pylon, wedge and wall obstacles, respectively. The positions of the cylindrical sensors with a diameter of 0.1 m (red diamond), the cylindrical sensors with a diameter of 0.25 m (blue five-pointed star) and the 1 m^2 measurement plate (green six-pointed star) are highlighted with arrows in the corresponding colors. (For interpretation of the references to color in this figure legend, the reader is referred to the web version of this article.)

beam at the front and the small wedge angle of 5 °, our DEM codes approximated the wedge with a flat front and parallel side walls, similar to a rectangular cross-section. As for the real measurement structure, we implemented the cylindrical pressure sensors of diameter 0.25 m protruding upstream from the beam at the same locations above the ground.

The third obstacle in Vallée de la Sionne is a concrete wall, 1.0 m in width and 4.5 m in height. There, the impact pressure is measured using two types of sensors. The first probe consists of a 1 × 1 m measurement plate centered at a height of 3 m above the ground. The second type involves three cylindrical pressure sensors identical to the ones used on the pylon, which are located in the middle of the wall at 1.5 m, 2.25 m and 3.75 m above the ground. These cylindrical pressure sensors were mounted in 2015. The DEM code reproduced the exact geometry and positions of the 1 × 1 m measurement plate and cylindrical sensors, although the cylindrical sensors are not present in measurements older than 2015.

2.2.2. Generic obstacles in DEM

To obtain a broader understanding of how impact pressure is affected by obstacle shape and size, we additionally simulated the interaction between avalanches and prismatic obstacles, including rectangular, circular and triangular cross-sections. Varied widths were considered. These geometries are commonplace in buildings, dams, cable car stations, protection structures and other infrastructures in avalanche-prone terrain. For all these obstacles, we chose a height of 5.7 m, which corresponded to the height of the highest velocity probe on the pylon (see Section 2.2.1). This height was sufficient to prevent the granular mass from overflowing the obstacle.

For the rectangular obstacles, the width w of the faces normal to the flow direction could be varied. The faces parallel to the flow direction were 1.6 m long in all simulations, which corresponded to the length of the pylon. For the triangular obstacles, we used wedges whose apex angle was $\alpha = 60°$ and which faced the flow. The wedge base was normal to the flow direction, and its width w could be altered.

Finally, for the cylindrical obstacles with circular cross sections, the width w was the diameter. For all cross-sections we used the following array of values: $w = [0.24, 0.6, 1.0, 3.0, 6.0]$ m. The widths $w \leq 1$ m matched the widths of the Vallée de la Sionne measurement obstacles.

In order to investigate how the impact pressure was distributed on the obstacles, the obstacles' surface was discretized into smaller areas. In the vertical direction, we divided all rectangular, triangular and cylindrical obstacles into 22 sections, each 0.26 m in height, which again corresponded to the vertical location of every second velocity sensor on the pylon (see Section 2.2.1). In the horizontal direction, we further divided the obstacle surfaces facing the granular flow into segments of equal widths. For most simulations the segment width was approximately 0.1 m. Only for the very narrow obstacles with $w = 0.24$ m, the segments were approximately 0.05 m wide to obtain a higher resolution of the impact pressure distribution. From left to right, Fig. 2 shows a perspective view of a rectangular, cylindrical and triangular obstacle with a width $w = 1$ m.

2.3. Avalanche scenarios

2.3.1. Generic avalanche scenarios in DEM

In our study, we selected four typical scenarios of flow avalanches based on the data collected over the last 20 years at the Vallée de la Sionne test site [29,68]. These include two scenarios of fast avalanches and two scenarios of slow avalanches. The fast-avalanche scenarios are mostly relevant for avalanches in the fully developed flow regime, whereas the slow-avalanche scenarios would better describe avalanches in the runout phase.

- **Cold shear flow regime** (also called cold dense flow regime in Köhler A. McElwaine and Sovilla [29]: this regime is characterized by a nonuniform vertical velocity profile, with velocity increasing substantially from the bottom (where it is close to zero) to the free surface of the flow (where it can be as high as 30 m/s in Vallée de la Sionne). This velocity profile implies that the flow experiences high frictional resistance at its base. Owing to high velocities, cold shear flows are often supercritical ($Fr > 1$) and are therefore considered inertial flows. The cold shear flow regime is also typical of the dense core in powder snow avalanches. The avalanche's dense layer is usually shallow, with flow depths of less than 4 m [29]. To model this scenario, we simulated a velocity profile increasing linearly from 0 m/s at the bottom to 30 m/s at the flow's free surface. We considered a flow depth of 2.5 m for all runs. Cold snow below −1 °C usually exhibits low cohesion (see Section 1), and we thus simulated a cohesionless granular material with the cohesive bond strength $\sigma_{coh} = 0.0$ kPa for this scenario.
- **Warm shear flow regime:** this regime refers to cases for which the vertical velocity profile may reach peak values of $v \simeq 25$ m/s. In contrast to cold snow, the snow in warm avalanches is considered to be highly cohesive, which may lead to large snow aggregation (clogging) within the avalanche [29,79,80]. Snow clogging is, however, counterbalanced by fragmentation induced

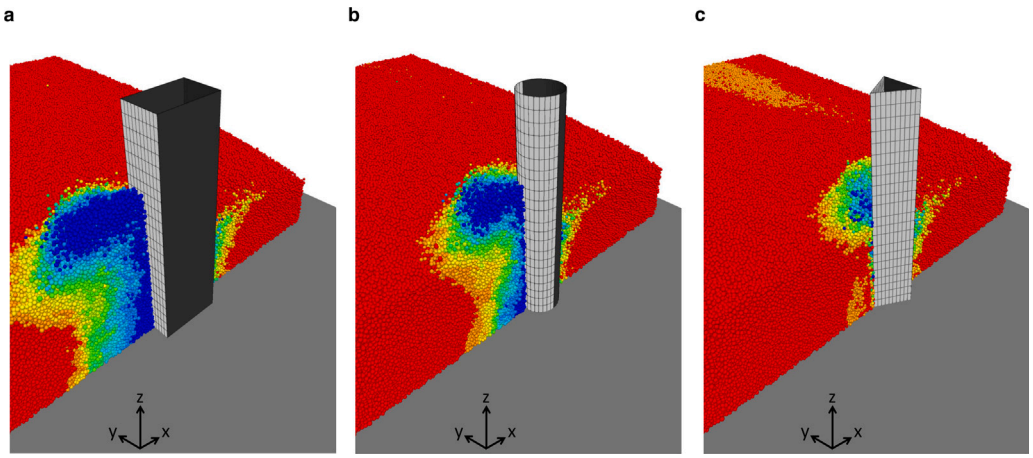

Fig. 2. Perspective views of the obstacles with a rectangular (a), circular (b) and triangular (c) cross-section. The black grid visualizes the discretization of the impact surface (shown in light gray). The obstacles are shown while interacting with an avalanche, which is cut vertically in the middle of the flow domain. The particles are colored according to their streamwise velocity, where red corresponds to 3 m/s and blue to 0 m/s. (For interpretation of the references to color in this figure legend, the reader is referred to the web version of this article.)

by collisions and high velocities within the flow. The vertical velocity profile is similar to that observed for the cold shear flow regime [29]. We simulated the warm shear flow regime with the same flow depth (2.5 m) and, despite the small velocity deviation, with the same vertical velocity profile as in the cold shear flow regime. To account for the high cohesion, we set the cohesive bond strength to $\sigma_{coh} = 10.0$ kPa. This cohesive strength value is higher than the back-calculated σ_{coh} for a range of typical warm avalanches documented by Sovilla et al. [9], but lower than for extremely cohesive avalanches [53].

- **Cold plug flow regime:** this regime is characterized by a low shear rate in the vertical velocity profile above the sliding surface [68]. Because the cold snow in this type of avalanche has little or no cohesion, a uniform velocity profile (plug flow) is observed when basal friction is low. On the contrary, a sheared velocity profile develops when the basal friction is sufficiently high. Plug flows typically occur in the tail of large cold snow avalanches, after the avalanche head has smoothed out the sliding surface, or in the runout of a cold, dry dense avalanche. Indeed, in this flow regime, velocities are usually lower than 10 m/s, which is often the case in the runout zone. Owing to the low velocity, cold plug flows are mostly subcritical ($Fr < 1$) and are, therefore, considered to be gravitational avalanches. In this flow regime, impact pressure is proportional to flow depth and independent of flow velocity [9]. To model this regime, we simulated a granular mass moving at an arbitrary velocity of 3 m/s uniformly across the flow depth. The flow was assumed to be cohesionless (cohesive bond strength $\sigma_{coh} = 0.0$ kPa). The flow depth was 2.5 m.
- **Warm plug flow regime:** this regime, defined by Köhler A. McElwaine and Sovilla [29], is often observed for avalanches with snow temperature close to 0°C. This flow regime is typical of dense wet snow avalanches. The snow in such avalanches is highly cohesive, and thus experiences clogging. The avalanche takes the form of a slow displacement of blocks gliding along the ground or snow cover [29,81]. To model this regime, we simulated a flow identical to the one in the cold plug flow regime, but with a cohesive bond strength of $\sigma_{coh} = 10$ kPa between the particles. Although the flow depth can reach 5 – 7 m [52], we still considered a flow depth of 2.5 m for the sake of comparison with the other flow regimes and to reduce the computational effort.

We summarize the properties of these four flow scenarios in Table 2a.

2.3.2. Vallée de la sionne avalanche scenarios in DEM

In order to test our DEM model, we compared simulated to measured impact pressure on the obstacles in Vallée de la Sionne. Hence, we needed to select recordings from the Vallée de la Sionne measurement archive, in which the three obstacles, located within an area of 16.5 m in radius, were hit simultaneously by the flow. For these real-world avalanche scenarios, we chose two typical examples including a warm plug flow regime avalanche and a cold shear flow regime avalanche, which are described below. To be able to compare impact pressure between real-world and simulated avalanche flows, we chose a vertical velocity profile in the simulations that came closest to the velocity profiles measured at the pylon.

- The February 1st 2013 avalanche (naturally released) is a typical example of the warm plug flow regime. Because the avalanche flow characteristics also evolve with time, we selected a sequence of 3 s from the complete recording with a duration of 4 minutes in the Vallée de la Sionne measurement database. In this selected time window, the avalanche's dense flow was moving at ~ 2.5 m/s and had a flow height of approximately 2.7 m. The sliding surface was roughly 1.2 m above the ground. We compared these measurements to simulations where a constant velocity of 2.5 m/s was imposed across the entire flow depth of 3 m. The cohesive bond strength was set to $\sigma_{coh} = 5.0$ kPa. This value corresponds to a moderate cohesion and is in the middle of the cohesion-less and highly cohesive scenarios defined in Section 2.3.1. Moreover, it is in the range of the back-calculated cohesive bond strength for which we to obtain a good agreement between computed and measured impact pressures for a number of warm plug flow avalanche events in Vallée de la Sionne [9,53].
- For the experimental data related to the cold shear flow regime, we selected measurements from an artificially released large powder snow avalanche on 8 March 2017. As done previously, we extracted a sequence of 1 s, during which the flow depth of the avalanche's basal flow was ~2.5 m. The velocity increased from 0 m/s at the ground to ~40 m/s at 2.5 m above the ground. For the comparison, we simulated a flow with a velocity profile increasing linearly from 0 m/s at the ground to 40 m/s at the free surface 2.5 m above the ground. For cold shear avalanches, we expected snow cohesion to be low and thus selected a cohesive bond strength of $\sigma_{coh} = 0.0$ kPa.

We summarize the two avalanche scenarios in Table 2b.

Table 2
Simulated avalanche flow scenarios. (For the color coded symbols refering to the different flow regimes in this table and throughout the text, the reader is referred to the web version of this article.)

Flow regime[a]		Typical application[b]	Velocity profile v	Cohesive bond strength σ_{coh}	Flow height h
(a) Generic avalanche scenarios in DEM					
gravitational	cold plug (|)	tail of dry flow avalanche runout	3 m/s constant	0.0 kPa	2.5 m
	warm plug (|)	wet flow avalanche track, runout	3 m/s constant	10.0 kPa	2.5 m
inertial	cold shear (/)	dry dense core of powder avalanche track	0–30 m/s shear	0.0 kPa	2.5 m
	warm shear (/)	wet dense core of powder avalanche track	0–30 m/s shear	10.0 kPa	2.5 m
(b) Vallée de la Sionne avalanche scenarios in DEM					
gravitational	warm plug (|*)	wet flow avalanche track, runout	~2.5 m/s constant	5.0 kPa	2.7 m
inertial	cold shear (/*)	dry dense core of powder avalanche track	0–40 m/s shear	0.0 kPa	2.5 m

[a]Distinction of flow regimes based on Fr and [28,29].
[b]Avalanche types and zones according to [20] and [82], respectively.

3. Comparison of simulated and measured impact pressure on obstacles of varied geometry

In this section, we show that our model was able to simulate the impact pressures on obstacles of different geometries and in different flow regimes. To that end, we compared simulated and recorded impact pressures by implementing pylon, wall and wedge obstacles – described in Section 2.2.1 – in our DEM code and matched the simulated velocity profile to the velocity measured at the pylon. The first and second rows of Fig. 3 show the simulated and measured impact pressures in the warm plug flow regime (|*) and the cold shear flow regime (/*), respectively, as described in Section 2.3.2.

The comparison exercise in Fig. 3 demonstrates a good general agreement between the simulated and measured impact pressures in the warm plug flow regime (|*) and the cold shear flow regime (/*). We observe that the model is able to capture the pressure differences measured by the different sensors at the three obstacles. This can be best seen by comparing the pressure on the wall with the square sensor of 1.0 m^2 area in the right column to the pressure values obtained for the cylindrical sensors with a diameter of 0.1 m. For the wall no measurements of the cylindrical sensors are available because these sensors were not yet mounted when this avalanche occurred in 2013 (see Section 2.2.1). However, the simulated pressure on the cylindrical sensors with a diameter of 0.1 m sensors on the wall is in good agreement with the pressure measured on the pylon with the same sensors and at the same height. In the warm plug flow regime (wall, |*), the simulated and measured pressures on the 1.0 m^2 sensor were considerably lower than the expected pressure for the smaller

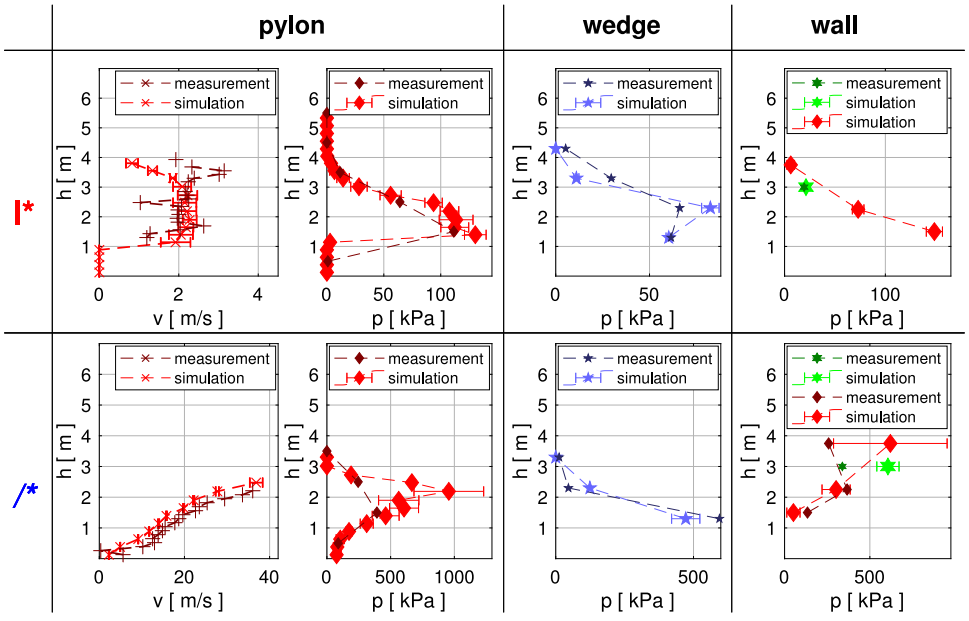

Fig. 3. Comparison of simulated and measured impact pressure on the Vallée de la Sionne obstacles. The plots in the first column show the measured (dark red) and simulated (light red) velocity at the pylon. The plots in the second, third and fourth columns show the measured and simulated pressure on the pylon, wedge and wall, respectively. The first and second rows show the impact pressure exerted by an avalanche in the warm plug and cold shear flow regime, respectively. The symbols represent the measured (dark colors) and simulated (light colors) impact pressure on the cylindrical sensors with diameters of 0.1 m (red) and 0.25 m (blue), as well as the 1 m^2 (green) sensor plate. These colors and symbols correspond to the illustration in Fig. 1. (For interpretation of the references to color in this figure legend, the reader is referred to the web version of this article.)

cylindrical sensors given by the linear interpolation of the values of the sensors at 2.25 m and 3.75 m above the ground.

In the middle (wall,|*), the pressure on lowest cylindrical sensor was lower than on the sensor at 2.2 m above the ground, which deviated from the proportionality of the pressure with the flow depth in the gravitational regime [e.g.,9,83,84]. However, this could be explained by the fact that the sensor at 1.2 m above the ground was already partially inside the avalanche deposit and therefore not impacted by the avalanche at full thrust.

In the cold shear flow regime (wall,/*), the simulated and measured impact pressures on the larger sensor were higher than on the small sensors. This was the opposite of what we observed in the warm plug flow regime (wall,|*). The qualitative agreement between simulations and measurements for the two different sensor types and in both flow regimes shows that the simulations were able to reproduce the measurements.

We did, however, observe differences between the simulated and the measured impact pressures. In the warm plug flow regime (wall,|*), the simulated pressure on the wedge obstacle increases at a moderately higher rate with flow depth and has a higher pressure peak compared to the measured pressure.

For the cold shear flow impacting the wall (wall,/*), the pressure on the highest cylindrical sensor at the wall 3.75 m above the ground was considerably higher in the simulation than in the measurement. In this case, the uppermost cylindrical sensor in the simulation was impacted by the dense flow. In the measurement of the powder snow avalanche, the sensor might already have been inside the powder cloud or the more dilute flow surrounding the dense layer, which would have exerted less pressure on the sensor.

The apparent discrepancy between the measured and simulated impact pressures on the pylon in the dense cold flow regime (/*), where the simulated pressure peak is about twice as high as the measured one (Fig. 3), is most likely due to the spatial resolution of the pressure measurements of 1 m. Probably, the maximum pressure peak occurred between the sensors positioned at 1.5 m and 2.5 m above the ground, and therefore was not measured. However, the simulated pressures at 1.5 m and 2.5 m agree well with the measured pressures.

4. Average impact pressure exerted on obstacles of different geometries

In Fig. 4a, we show the simulated impact pressures on obstacles of rectangular (□), circular (○) or triangular (△) cross-section of varied width exerted by an avalanche in the cold plug (|) and warm plug (|) flow regime scenarios defined in Table 2a. In both flow regimes, the impact pressure was highest on the rectangular cross-section. On average, the impact pressure on the circular and triangular cross-sections was 17% and 43% lower, respectively, than the pressure on the rectangular cross-sections.

We also observed that the impact pressure p_x decreased with increasing obstacle width for all cross-sections. The impact pressure exerted by a cold plug flow decreased by only 2.7 kPa from $p_{x,w=3\,\mathrm{m}}$ to $p_{x,w=6\,\mathrm{m}}$, while the pressure decreased by 4.6 kPa from $p_{x,w=0.24\,\mathrm{m}}$ to $p_{x,w=0.6\,\mathrm{m}}$ with a much smaller change in w. The decrease in the rate of change in p_x for increasing w indicates that from a certain w value, p_x no longer decreased significantly with further increases in w. As the impact pressure decrease rate with increasing w was already low for $w = 6$ m, we assumed that the pressure decrease for $w > 6$ m was negligible. Hence, we used the impact pressure on the widest obstacle $p_{x,w=6\,\mathrm{m}}$ as an approximation of the impact pressure on wider obstacles. In order to quantify the pressure increase on a narrow obstacle compared with that on a wide obstacle in Fig. 4b, we divided the impact pressures of varied widths p_x by the impact pressure on the widest obstacle $p_{x,w=6\,\mathrm{m}}$ of the same cross-section type and flow regime.

Fig. 4b shows that the pressure decrease in the cold plug flow on obstacles of increasing width was similar for all cross-sections.

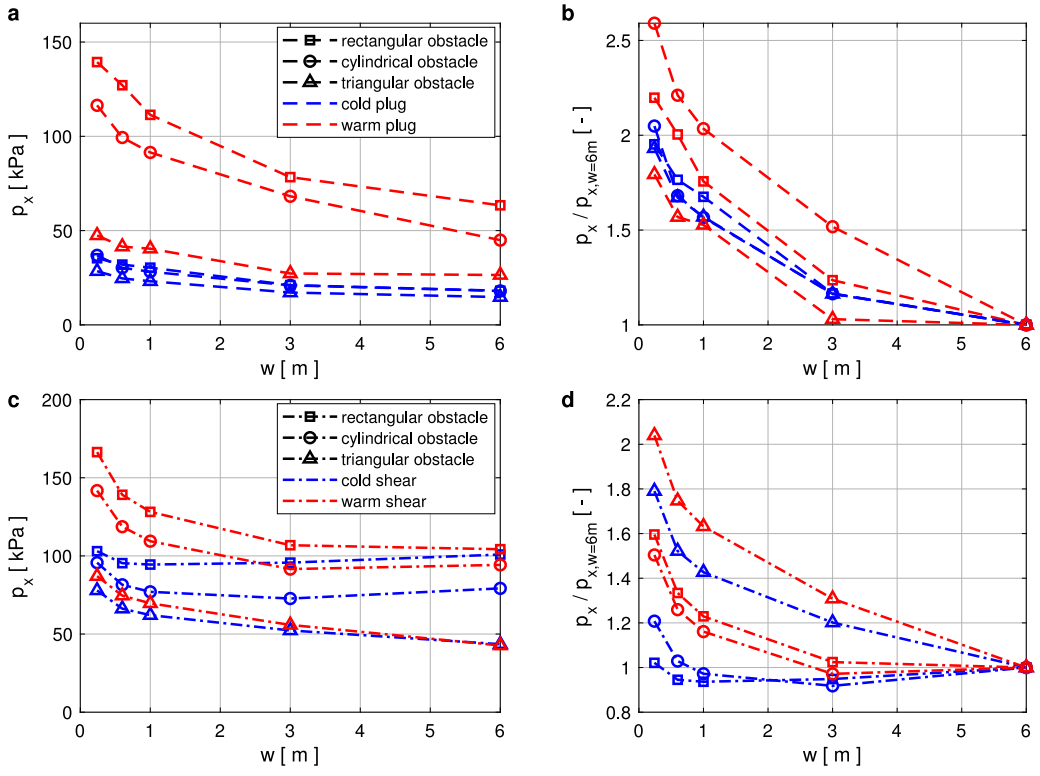

Fig. 4. Dependence of impact pressure p_x on obstacle geometry and width w. Panel a shows the impact pressure exerted by a cold plug (dashed, blue) and a warm plug (dashed, red) avalanche flow. Panel c shows the impact pressure exerted by a cold shear (dash-dotted, blue) and a warm shear (dash-dotted, red) avalanche flow. Panels b and d show the impact pressure for obstacles of varying width w relative to the pressure on the 6 m wide obstacle of the same geometry and flow regime in the gravitational and inertial flow regimes, respectively. (For interpretation of the references to color in this figure legend, the reader is referred to the web version of this article.)

$p_{x,w=0.24\,\mathrm{m}}$, $p_{x,w=0.6\,\mathrm{m}}$, $p_{x,w=1\,\mathrm{m}}$ and $p_{x,w=3\,\mathrm{m}}$ were on average 2.0, 1.7, 1.6 and 1.2 times higher, respectively, than $p_{x,w=6\,\mathrm{m}}$. In the warm plug flow regime we observed the highest ratio $p_{x,w=0.24\,\mathrm{m}}/p_{x,w=6\,\mathrm{m}} = 2.6$ for the circular cross-section and the lowest value $p_{x,w=0.24\,\mathrm{m}}/p_{x,w=6\,\mathrm{m}} = 1.8$ for the triangular cross-section. Hence, the differences between the pressure ratios of different cross-sections in the warm plug flow regime (|) were slightly larger than the values in the cold plug flow regime (|).

Fig. 4c shows the simulated impact pressures on obstacles of varied width exerted by an avalanche in the cold shear (/) and warm shear (/) flow regimes. Similar to in panel a, the impact pressure was highest on the rectangular obstacles, while 22% and 45% less impact pressure was exerted on the cylindrical and triangular obstacles, respectively. The impact pressure increase from the cold shear (/) to the warm shear (/) flow regime due to an increase in cohesive bond strength was of a factor 1.7 on average. This was considerably lower than the impact pressure increase due to an increase in cohesive bond strength of a factor of 3.2 in the gravitational regime (|,|).

For all obstacles impacted by the cold shear (/) and warm shear (/) flow avalanche, the pressure decreased for $0.24\,\mathrm{m} \leq w \leq 1\,\mathrm{m}$. For $w > 1$ m the impact pressure either decreased further or increased slightly, depending on the geometry and flow regime.

In Fig. 4d, we scaled p_x by $p_{x,w=6\,\mathrm{m}}$ of the same geometry and flow regime, similar to the gravitational flows, although the qualitative trend in p_x was not consistent. Panel d shows more clearly that in the inertial flows (/,/), the dependency of the impact pressure on the obstacle width was generally lower than for the gravitational flows (|,|).

5. Pressure distribution on obstacles of different geometries

In this section, we present how the impact pressure was distributed on the obstacle surface. For the tested obstacle of width $w = 1$ m, in Fig. 5, we visualize the distribution of the impact pressure exerted by avalanches of four flow regimes (see Section 2.3.1) on obstacles with different cross-sections.

In the first two columns of Fig. 5, we observe that the impact pressure was largest at the bottom of the avalanche flow for the plug flow regimes (|,|). For the cold shear flow regime (/) in the third column, the impact pressure was highest at the flow surface, 2.5 m above the ground. In the warm shear flow regime (/), in the right column, the highest pressure was also located near the flow surface, but the pressure peak was more spread out towards the ground compared with in the cold shear regime (/).

When we calculated the height z_R at which the resulting force on the obstacle is applied, which is relevant for computing the bending moment, we observed that z_R did not vary significantly for the three different obstacle geometries. On the contrary the vertical position of the resulting force strongly depends on the flow regime. In the two plug flow regimes (|,|), we found $z_R = 0.32h$, regardless of the cohesive bond strength. By contrast, we found $z_R = 0.6h$ in the cold shear flow regime (/), $z_R = 0.52h$ and in the warm shear flow regime (/).

In the horizontal direction, the pressure distribution was variable for the different geometries and flow regimes. In order to analyze the horizontal pressure distribution more closely in Fig. 6, we plotted the impact pressure as a function of the y coordinate transverse to the flow direction at different heights z. To improve the visibility of

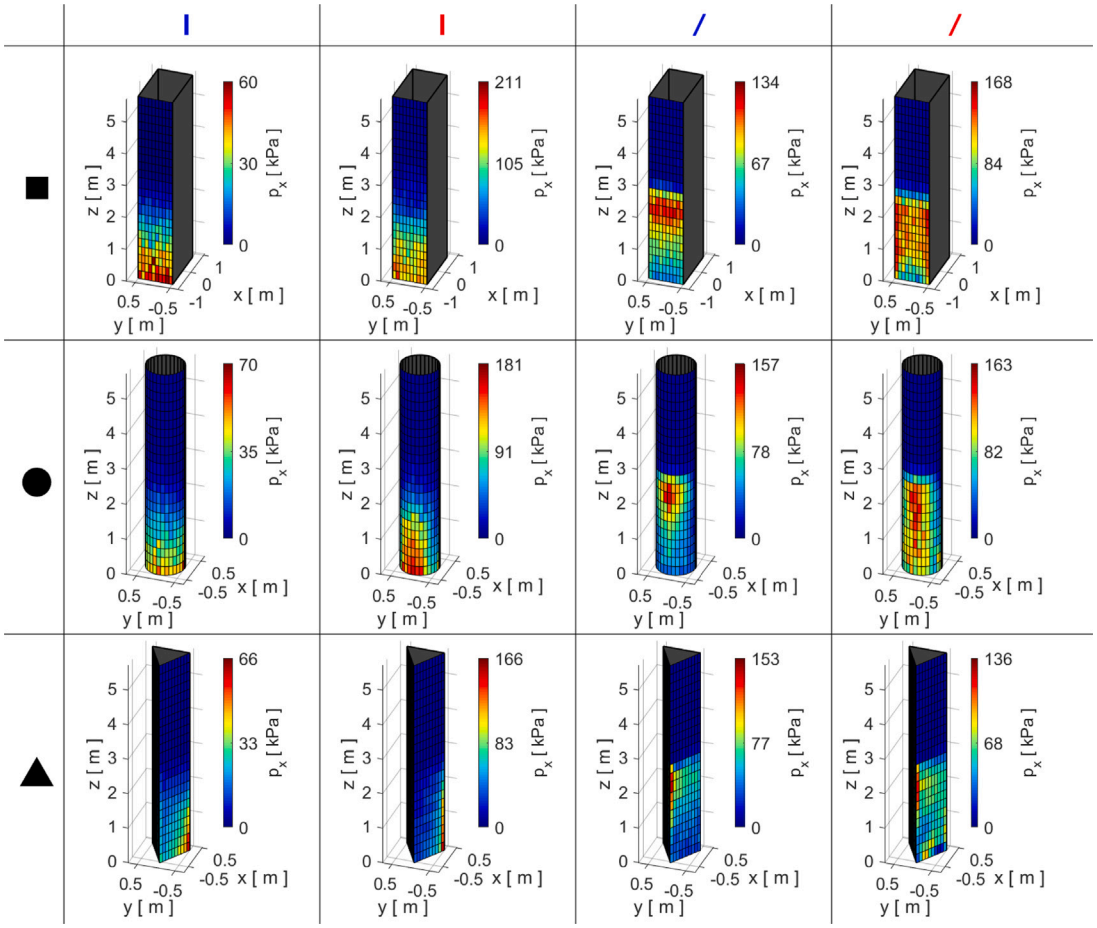

Fig. 5. Impact pressure distribution on the discretized impact surface of the prismatic obstacles ($w = 1$ m) with a rectangular, circular or triangular cross-sections. From left to right the columns show the pressure distribution in the cold plug, warm plug, cold shear and warm shear flow regimes. The colors represent the average impact pressure magnitude on the respective surface. (For interpretation of the references to color in this figure legend, the reader is referred to the web version of this article.)

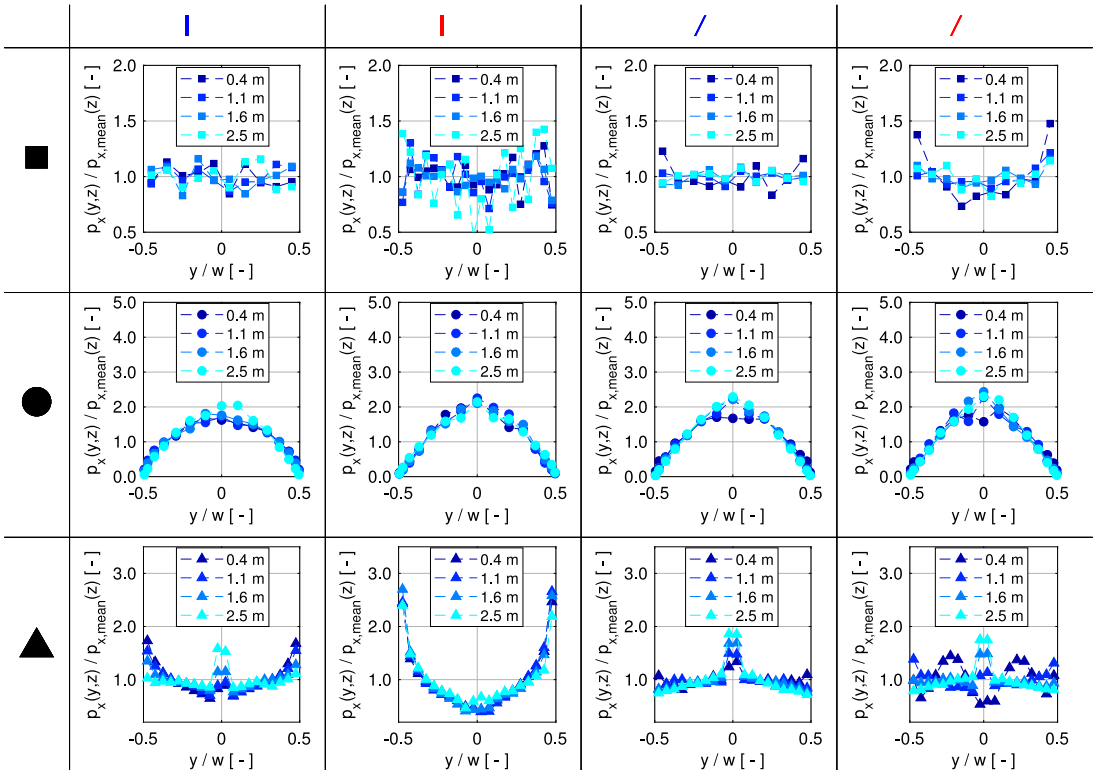

Fig. 6. Horizontal pressure distribution on obstacles with $w = 1$ m normalized by the average pressure at the respective height. The first, second and third rows show the pressure distribution on the obstacles with rectangular, circular and triangular cross-sections, respectively. From left to right the columns show the pressure distribution in the cold plug, warm plug, cold shear and warm shear flow regimes.

the horizontal pressure variations, we scaled the local impact pressure $p_x(y, z)$ by the average pressure $p_{x,mean}(z)$ at the respective height and the y coordinate with the width w of the obstacle.

In the first row in Fig. 6, we observe that the impact pressure on the rectangular obstacle (□) exerted by the cold regimes (|,/) was evenly distributed in the y-direction. In contrast, the impact pressure exerted by the warm regimes (|,/) was up to ∼ 1.5 times higher at the outer edges than in the middle of the obstacle. In the warm shear regime (/), these pressure concentrations at the edges were most pronounced at the bottom of the flow.

For the circular cross-sections (○) in the middle row, the pressure distribution showed no significant differences for the four flow regimes tested. The impact pressure was highest in the middle of the obstacle, where the flow impacted the obstacle at a right angle, and was lowest at the sides where the obstacle surface was tangential to the flow.

Depending on the flow regime and flow depth, the horizontal pressure distribution on the triangular obstacles (△) in Fig. 6 shows pressure concentrations both at the obstacle outer edges and at the leading edge. A pressure peak at the leading edge of ∼ 2 times the average pressure was present in most cases (|,/,/), but not in the warm plug regime (|) or near the ground for the warm shear regime (/). A pressure peak at the outer edges of the obstacle, where the pressure was up to ∼ 2.5 times higher than the average pressure, occurred across the whole flow height in the warm plug regime (|) and was most pronounced near the ground in the cold plug regime (|).

6. Impact pressure calculation

Here, we propose a physics-based and practice-oriented method for estimating C_D values depending on the obstacle geometry and the avalanche flow characteristics. In Section 6.1, we present a method for estimating C_D for cohesionless avalanches (e.g., |,/), which are often relevant in practice, as they are representative of dry fast avalanches in the avalanche track and runout. In Section 6.2, we show how the impact pressure increase caused by an increase in cohesive bond strength (e.g., |,/) can be calculated.

6.1. Estimation of drag coefficients for cohesionless avalanches

Based on similar findings in previous studies [6,8,85,86], we propose a physics-based definition of the drag coefficient C_D, similar to Eq. (4), as follows:

$$C_D = C_{geo}\, C_r = C_{geo}\left(1 + \frac{K}{Fr^2}\right) \tag{8}$$

where we first divide C_D into two factors [8]: (1) C_{geo}, which is solely related to the geometry of the obstacle, and (2) C_r, which depends on the flow regime of the avalanche. Furthermore, we rewrite the coefficient C_r according to Eq. (6) [7,85].

The average impact pressure of an avalanche with a flow depth h and velocity v can be calculated according to Eq. (9):

$$p_{x,calc} = C_D \frac{\rho}{2} v^2 = C_{geo} \frac{\rho}{2} v^2 + \zeta \rho g \frac{h}{2} \tag{9}$$

where we use the definition of $Fr = v/\sqrt{g\,h}$ and set $\zeta = C_{geo} K$ to obtain a formulation similar to that used by Sovilla et al. [52].

For the gravitational plug flow regime (|) in Fig. 4a, we find that the impact pressure decreased for obstacles of increased width for all geometries. Hence, as shown by Eq. (10), we further decompose the geometry factor C_{geo} into a coefficient C_o considering only the obstacle's geometrical shape and a coefficient $C_w = p_x/p_{x,w=6\,\mathrm{m}}$ depending on the obstacle width, as presented in Fig. 4.

For the impact of avalanches in the inertial shear flow regime (/) in Fig. 4c, the width influence was not monotonic or similar for all geometries. For lack of a better understanding of the physical processes involved, and given the qualitative trend exhibited by the width influence on the pressure in these regimes, we set $C_w = 1$ in the cold shear (/) flow regime for all w:

$$C_{geo} = C_o\, C_w \tag{10}$$

To estimate the geometrical part C_o of the drag coefficient C_{geo} of an obstacle, for which C_o is not known *a priori*, we propose the heuristic Eq. (11). This method is based on the concept that the resistance to the flow offered by a flat body scales with the cosine of its angle to the flow's direction transverse (the y-direction in our setup). Hence, we discretize the obstacle's impact surface into n piecewise straight segments at an angle θ_n and of width d_n and calculate C_o as the sum of the weighted contributions of the individual straight segments as in Eq. (11). A prerequisite for applying Eq. (11) is that the obstacle's impact surface facing the upstream direction of the flow must be convex.

$$C_o = 1 + \frac{1}{w}\sum_n \cos\theta_n \, d_n \tag{11}$$

From Eq. (11), we can identify two limiting cases: (1) $C_o = 1$ for an infinitely narrow object parallel to the flow, and (2) $C_o = 2$ for an obstacle of finite width with a flat face at a right angle to the flow direction. Fig. 7a illustrates Eq. (11). Fig. 7b shows examples calculations of C_o for the geometries considered in this study.

The remaining factor to be determined in Eq. (8) is K, which is associated with the depth-dependent impact pressure contribution of gravitational avalanches [9]. In the gravitational flow regime, the impact pressure on the structure predominantly originates from the material compression inside the flow region, which is influenced by the presence of the obstacle [53,55,56]. The compression of the granular material is mainly caused by particle jamming due to the resistance to the flow offered by the obstacle. Because flow resistance depends on the obstacle geometry, we use C_o as a proxy for how much the material is jamming upstream of the obstacle rather than being deflected. Confined compression tests on a granular material with the same properties as in this study have shown that the axial stress scales approximately with the square of the particle inter-penetration, which corresponds to the material compression at the particle scale [56]. Hence, as an approximation, we set the factor $K = C_o$ such that the second term of the regime-dependent coefficient C_r scales with C_o^2. Because in the compression tests the lateral stresses are proportional to the normal stress, we followed Faug [85], where K corresponds to the *earth pressure coefficient*, and used the approximation $K = C_o$. Finally, using $K = C_o$, the drag coefficient C_D can be estimated using Eq. (12):

$$C_D = C_{geo}\, C_r = C_{geo} + \frac{C_{geo}\, K}{Fr^2} = C_o\, C_w + \frac{C_o^2\, C_w}{Fr^2} \tag{12}$$

6.2. Impact pressure exerted by cohesive avalanches

Snow cohesion in an avalanche is only relevant for the flow behavior and the impact pressure above a certain cohesion threshold [28,53,87]. The threshold is not a constant, but depends on the balance between the collisional forces, proportional to the flow velocity, and the cohesive strength between the particles. Below the threshold value, the flow exhibits a predominantly cohesionless behavior, because the collisional forces break snow aggregations apart. Above the threshold value, the avalanche snow is cohesive enough to aggregate more snow particles than the collisional forces can break. This interplay between collisional and cohesive forces, which also governs the impact pressure increase due to an increase in cohesive bond strength, can be captured by considering the Bond to Froude number ratio $q_{Bo,Fr} = Bo/Fr$ [53]. The dimensionless Bond number $Bo = \sigma_{coh}/p_{conf}$ is the cohesive bond strength σ_{coh} divided by the confining pressure p_{conf} [88], which is the vertical component of the local stress tensor.

As already demonstrated in our earlier paper [53], the impact pressure exerted by a cohesive avalanche $p^*_{x,calc}$ can be simply calculated according to Eq. (13), by multiplying a factor $f_{coh}(q_{Bo,Fr})$, based on the ratio of the Bond number, by the impact pressure exerted by a cohesionless flow with the same flow height and velocity $p_{x,calc}$:

$$p^*_{x,calc} = p_{x,calc}\, f_{coh}(q_{Bo,Fr}) \tag{13}$$

We assume that f_{coh} varies slightly depending on the obstacle geometry. However, many simulation runs with varying v and σ_{coh} are needed to obtain f_{coh} as a function of $q_{Bo,Fr}$ for a specific geometry, making it cumbersome to find f_{coh} for all geometries in this study. Hence, as an approximation, we use the scaling available from our earlier work [53] using the Vallée de la Sionne pylon, which we fit with Eq. (14):

$$f_{coh} = c_1/(c_2 + q_{Bo,Fr}) + c_3 \tag{14}$$

where $c_1 = -3.6$, $c_2 = 1.5$ and $c_3 = 3.4$ are the fitting parameters.

7. Comparison of calculated impact pressure with simulations and measurements

7.1. Cohesionless avalanches

Using the method for the estimation of C_o, C_w and K described in the previous section, we calculate the impact pressure $p_{x,calc}$ of a cold plug flow (|) and a cold shear flow (/) on obstacles of varied geometry. We compare the calculated and simulated impact pressure $p_{x,DEM}$, as shown in Fig. 8.

For the calculation of $p_{x,DEM}$ and the associated C_D, we choose C_w according to the pressure ratios $p_x/p_{x,w=6\,\mathrm{m}}$ of the cold plug flow (|) in Fig. 4b and assume $C_w = 1$ in the cold shear regime (/) (see). C_o is calculated using Eq. (11).

In Fig. 8, we observe that the calculated impact pressure agrees relatively well with the simulated values. For the impact pressures exerted by the cold plug flow (|) in the first row, the pressure on the rectangular obstacle is slightly overestimated, while the pressure on the cylindrical and the triangular obstacles is slightly underestimated for all obstacles widths. In the inertial cold shear flow regime (/), the influence of obstacle width on the pressure is not captured because we assume $C_w = 1$ in this regime for all w. The mean relative error between the simulated and the calculated pressure is 12% in the cold plug flow and 15% in the cold shear flow.

In the cold plug flow regime (|), the flow depth-dependent gravitational pressure contribution (dark blue area) is dominant, with a

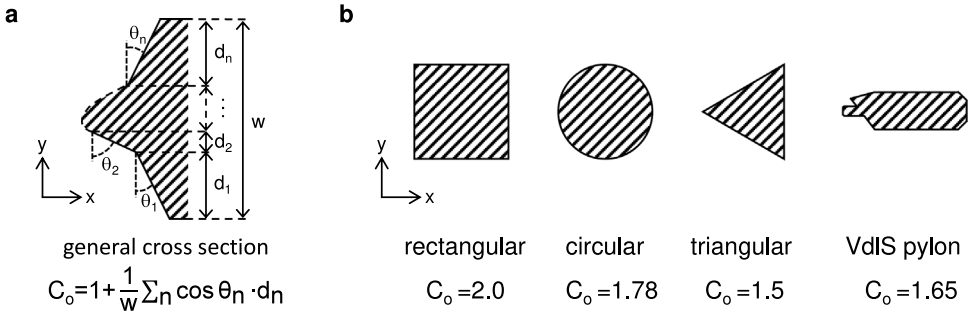

Fig. 7. C_o estimation based on Eq. (11) for a general cross-section in panel a and for selected cross-sections in panel b. VdlS = Vallée de la Sionne.

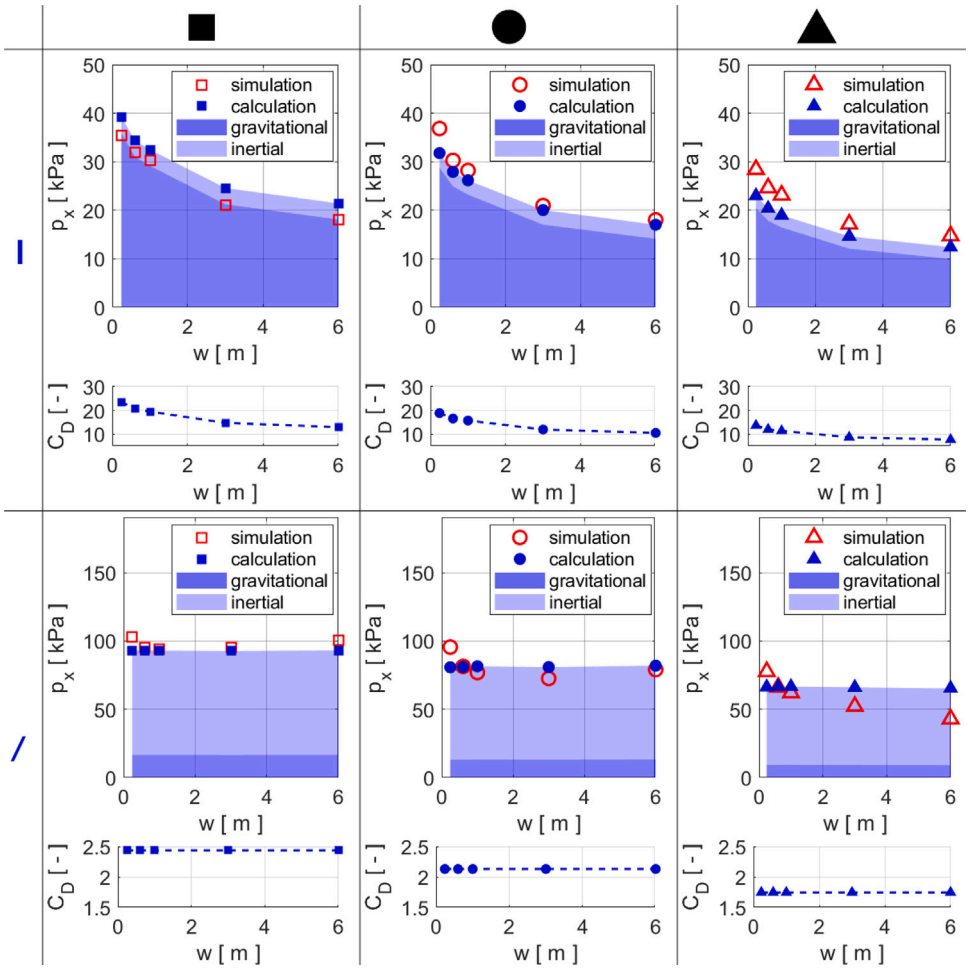

Fig. 8. Comparison of simulated impact pressure (red symbols) and pressure calculations (blue symbols) using Eqs. (1) and (12) (top in each row), as well as calculated C_D (bottom in each row), for varying obstacle widths w. The first, second and third columns show the pressure comparison for the obstacles with rectangular, circular and triangular cross-sections, respectively. The calculated C_D and the pressure exerted by an avalanche in the cold plug (first row) and the cold shear (bottom row) flow regime are shown. In the pressure plots (top in each row), the dark blue shaded areas represent the calculated gravitational pressure contribution, where the impact pressure is proportional to the flow depth, while the light blue shaded areas represent the calculated inertial contribution, where the impact pressure is proportional to velocity squared. (For interpretation of the references to color in this figure legend, the reader is referred to the web version of this article.)

share of 85% of the total calculated impact pressure. Using Eq. (9), we can calculate the proportionality factor $\zeta = C_o^2 C_w$ is associated with the gravitational pressure contribution from the data in Fig. 8. The corresponding ζ values in Fig. 8 are $2.3 \leq \zeta \leq 7.9$, where the highest value corresponds to the narrowest rectangular obstacle and the lowest value corresponds to the widest triangular obstacle.

If we calculate the C_D values according to Eq. (12) for all scenarios depicted in Fig. 8, we obtain values in the 7.6–23.6 range for the cold plug (|) and in the 1.7–2.4 range for the cold shear flow regime (/), as shown in Fig. 8.

In the inertial cold shear flow (/) the pressure contribution proportional to velocity square (light blue area) has a share of 80% of the total calculated impact pressure. Hence, in this regime the geometry dependent coefficient C_{geo} prevails.

7.2. Real avalanche scenarios

To assess how realistic the drag coefficient is for a real-world avalanche, we calculate the vertical impact pressure profile for the warm plug (|*) and cold shear (/*) avalanches on the Vallée de la Sionne obstacles and compare it to the measured and simulated impact pressure in the real avalanche scenarios (|*,/*) described in Section 2.3.2. Again, we estimate C_D values in the cohesionless flows, using the method proposed in Section 6.1 to calculate the average impact pressure. In the warm plug regime (|*), we consider the impact pressure increase due to an increase in cohesive bond strength by calculating the pressure increase factor $f_{coh} = 1.94$ according to Section 6.2, using the scaling law from our earlier work [53] with $Bo = 0.50$ and $Fr = 0.49$.

In order to calculate the vertical pressure profile, we calculate the gravitational and inertial pressure contribution from Eq. (9) individually. Subsequently, we use the proportionality of the pressure with the flow depth in the gravitational regime [e.g.,9,83,84] and with velocity squared in the inertial regime [e.g.,35–38,61,89] to determine the vertical distribution. Further information on how we calculated the impact pressure profiles is provided in the Supplementary Material S.3.

In Fig. 9, we plot the simulated and measured impact pressures from Fig. 3, and we compare it to the pressure calculations.

Fig. 9 shows that the calculated vertical impact pressure profiles qualitatively agree well with the simulated and measured pressure profiles. For the cold shear flow regime (/*) impacting the wedge obstacle, the comparison is made difficult by the fact that the measured dense flow at this particular obstacle was probably below the sensor at 2.3 m above the ground, leaving only the lowest sensor at 1.3 m measuring the impact pressure of the dense flow.

Although we obtain fairly good qualitative agreement between most computed and measured pressure calculations, we observe significant differences between calculations and measurements for two scenarios.

The calculated impact pressure is 34% lower than the measured pressure for the pylon impacted by the warm plug flow avalanche (|*) and 42% lower for the wedge impacted by the cold shear flow (/*).

The reason for this difference for the pylon may originate from the choice of C_w based on the assumption that the pylon's overall width $w = 0.6$ m is relevant for the impact pressure [52]. Actually, the sensors at the pylon have a diameter of only 0.1 m and protrude upstream into the flow. Hence, it is difficult to determine which w is relevant when choosing C_w.

For the cold shear flow (/*) impacting the wedge, the error probably originates from our assumption that $C_w = 1$ for all obstacles impacted by inertial flows. However, in Fig. 4 we observe that the impact pressure on the narrow obstacles with the same width as for the wedge ($w = 0.24$ m) is greater than for the other obstacle widths.

As indicated in the legend, the calculated C_D used for the pressure estimates range from 23.9 to 40.0 in the warm plug flow (|*) and from 1.8 to 2.3 in the cold shear flow regime (/*), respectively.

8. Discussion

8.1. Avalanche impact pressure on obstacles of varying geometry

When comparing the simulated and measured impact pressures in Fig. 3, we find that the DEM code performs well at computing the pressure differences between obstacles and sensors of varied geometry for different flow regimes. The discrepancies observed in Section 3 between simulations and measurements can be explained by the complex and time-dependent nature of real-world snow avalanches when interacting with obstacles. Examples of this complexity include deposition processes upstream of the obstacle and the coupling between the avalanche's dense and dilute flow phases.

Fig. 3 shows that not only the impact pressure, but also the simulated vertical velocity profiles are very similar to the measured ones. This confirms that imposing a linearly increasing shear velocity profile (Section 2.3.2) for the inertial flows agrees with the findings of Silbert et al. [90] for granular flows on rough inclined planes. Silbert et al. [90] find, that low inclinations close to the flow–no-flow threshold produce slow and continuous granular flows, for which "the rheology is not Bagnold-type, rather the velocity profile is better approximated by a linear relationship with depth $v_x(z) \sim z$". However, although the linearly increasing velocity profiles match relatively well in the examples in Fig. 3, it has to be noted that in other cases more complicated velocity profiles may be observed in avalanches, e.g. at VdlS [91].

Consistent with findings from earlier studies [e.g.,53,87], panels a and c in Fig. 4 show that snow cohesion can strongly amplify the impact pressure, particularly in the gravitational regime. It is worth noting that the impact pressure is not limited to the values simulated in our cohesionless or cohesive flow scenarios. The impact pressure varies with σ_{coh} from the blue curves (|,/) up to the red curves (|,/) for any given obstacle geometry and width. If σ_{coh} is higher than assumed in our scenarios, the pressure values may even exceed the red curves.

As a consequence, computations of p_x are fraught with uncertainty for cohesive avalanches: its value depends crucially on the choice of the cohesive bond strength σ_{coh}. In the absence of hard information on the link between snow temperature and cohesion, no upper limit of σ_{coh} is known. Values as high as $\sigma_{coh} = 15.6$ kPa have been fitted for an avalanche from Vallée de la Sionne [53], and even higher values are possible.

Fig. 4a and c also show that the simulated impact pressure depends heavily on the obstacle geometry. The rectangular obstacles experience the highest impact pressure, and the impact pressure on the triangular obstacles is on average ~ 45% lower. The pressure on the rectangular obstacles is not only higher than the impact pressure on the triangular obstacles, but also shows more dependence on the flow regime, e.g., if the cohesive bond strength increases. Hence, for construction in locations where little is known about the behavior of extreme avalanches, the triangular cross-section has the advantage of experiencing lower absolute pressures and smaller pressure variations in different avalanche scenarios compared with other geometries.

In Fig. 4, we further observe that the impact pressure exerted by gravitational flows (|,|) decreases similarly for all obstacle cross-sections with increasing w. This finding is consistent with the qualitative behavior observed in many contexts where obstacles or intruders move relative to a surrounding medium at subcritical speeds [e.g.,10,56,92].

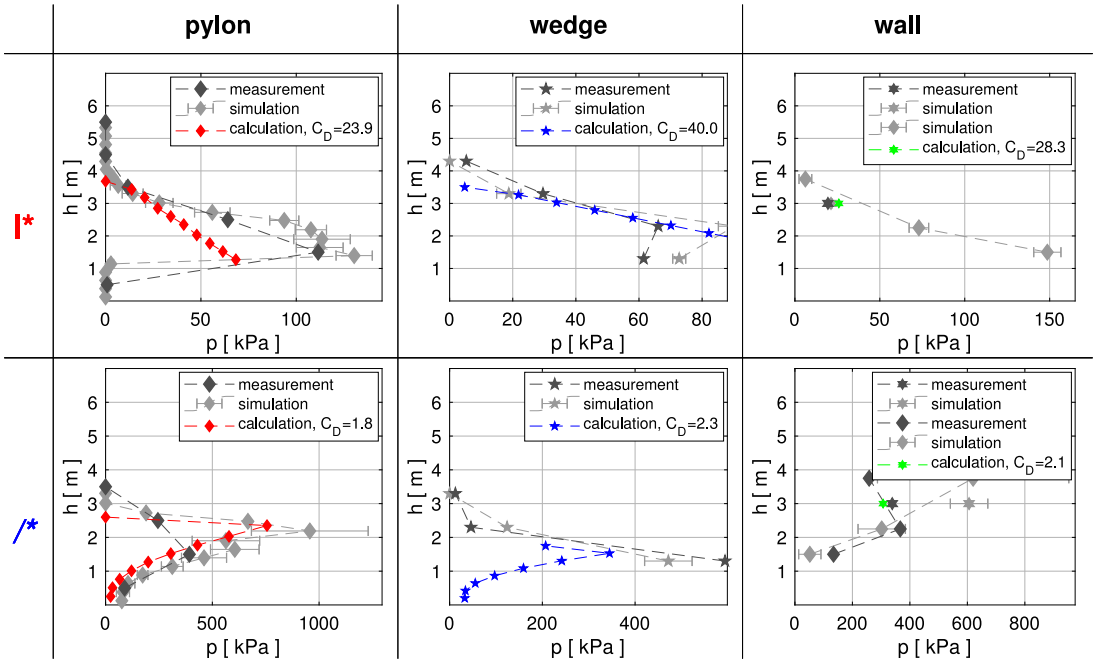

Fig. 9. Comparison of calculated (colors) with simulated (light gray) and measured (dark gray) impact pressure profiles on the Vallée de la Sionne measurement obstacles. From left to right the columns show the comparison for the pylon, the wedge and the wall obstacle. The first and second rows show the impact pressure exerted by an avalanche in the warm plug and cold shear flow regime, respectively. The colors and symbols correspond to the illustration in Fig. 1. (For interpretation of the references to color in this figure legend, the reader is referred to the web version of this article.)

In an earlier study [56], we tentatively proposed that decreasing p_x is caused by increasing shear dilation in the flow around obstacles of increasing w, but the physical origin of this trend has yet to be established with certainty.

For gravitational avalanches, we observe that the impact pressure tends to decrease with increasing w, a feature that is of particular relevance to understanding what may happen in the runout of avalanches with a long return period, in which case dwellings would be the obstacles. Special attention should be paid to the warm plug flow regime. In Vallée de la Sionne, avalanche flow depth can be as large as 5–7 m [52]. Due to the greater flow height, this would result in pressure $p_x \sim 2.5$ times higher than the impact pressure simulated for the warm plug flow regime (|) in this paper. Some extreme avalanches may exhibit snow cohesion greater than the maximum cohesive bond strength considered in this article, which would lead to an even higher impact pressure. In the gravitational regime the impact pressure is linearly distributed across the flow depth (see Fig. 5) [9,83,84]. As the highest pressures are located at the flow base, reinforcing the foundation and lower part of buildings is recommended, e.g. particularly for buildings at low altitudes, where gravitational avalanche flows are most likely.

This behavior of gravitational avalanches contrasts with what is observed for the inertial flow regime in Fig. 4c: the impact pressure decreases for all cross-sections and flow regimes (/,/) for $w \leq 1$ m. For $w > 1$ m the qualitative trend of p_x is somewhat unclear and probably negligible. Fig. 4d indicates that overall the influence of w on p_x is weaker in the inertial flow regime (/,/) than in the gravitational flow regime (|,|) in panel b. For narrow obstacles, such as masts of chair lifts or power lines in the avalanche track, the influence of w on p_x is admittedly lower, but the position of such obstacles in the avalanche flow zone makes the probability of an inertial flow regime (/,/) very high.

In Section 5, we observed that the height z_R at which the resulting force on the obstacle is applied, depends on the flow regime but not on the obstacle geometry, for the geometries considered in our study. The most critical scenario is the cold shear flow regime (/). In this regime z_R is largest because the impact pressure increases with increasing velocity [35–38,61], which is highest near the flow-free surface. As a consequence, obstacles experience higher bending moments in this regime than in the plug flow regimes, where the highest pressures are observed at the flow base. Note that in our simulations we do not take into account the presence of the snow cover or avalanche deposits of preceding avalanches, which may increase the height of the basal sliding surface of the avalanche and consequently increasing also z_R. Hence, for the calculation of the bending moment, in practice the thickness of the snow cover below the basal layer of the avalanche has to be added to the z_R values presented in Section 5. The challenge lies in estimating this thickness, which depends on many factors such as the amount of snow precipitation, blowing snow, rain and sun at a specific location, deposits of preceding avalanches and the erosion depth of the impacting avalanche. All these factors are difficult to predict and vary considerably for any specific location of an obstacle.

Computation of inertial flows is also fraught with higher uncertainty than for gravitation flows, owing to the pressure dependency on the velocity squared. In our simulations, we generated velocities as high as ~40 m/s, which is consistent with the fastest velocities observed for dense flows in Vallée de la Sionne. As for dense flows, the maximum velocity depends on the avalanche track topography, and higher values are likely in other sites (Gubler et al. [93] cites values as high as 60 m/s).

Fig. 6 shows that, depending on the flow regime, impact pressure is not distributed homogeneously on the obstacle surface: at the outer edges and at the leading edge in the middle of an obstacle, it is up to ~ 2.5 times higher than the average pressure. Local structure reinforcement can be considered an appropriate countermeasure to this punching effect.

8.2. Estimation of the drag coefficient

As the drag coefficient C_D varies smoothly between the subcritical and supercritical regimes, Eq. (8) allows us to go beyond the classic dichotomy between gravitational and inertial avalanches. This possibility is essential for a physics-based estimation of C_D because avalanches can undergo flow regime transitions and multiple flow regimes may coexist in a single avalanche [29,94]. With Eq. (8) the impact pressure can be interpreted as the sum of a velocity squared and a flow depth-dependent contribution, as suggested in a number of studies on snow avalanches and other gravity-driven flows [e.g.,4,52,95]. In Eq. (8), the Froude number determines the relative importance of the inertial and gravitational contributions to impact pressure:

- For subcritical flows ($Fr < 1$), the contribution weighted by K, which is related to the gravitational contribution, is the dominant term;
- For supercritical flows ($Fr > 1$), K/Fr^2 becomes smaller whereas C_{geo} becomes larger.

In addition to the Froude number Fr, the parameters C_o, C_w and K have to be determined to calculate C_D (see Eq. (12)). In a previous study [56], we showed that for the gravitational regime, impact pressure depends on material compression in the domain of influence around the obstacle, and based on the present study, we can assume that $K = C_o$ (see Section 6.1), which reduces the number of variables to only two (C_w and C_o).

For the width-dependent coefficient C_w, we use $p_{x,w}/p_{x,w=6\,\mathrm{m}}$ factors derived from our simulations in the gravitational regime (Fig. 4b), but this may be a source of error because we neglect a further decrease in p_x for $w > 6$ m. In the absence of knowledge on the physical processes underlying the dependency of p_x on w, we assume $C_w = 1$ in the inertial regime.

To calculate the coefficient C_o, we propose the heuristic Eq. (11), which provides C_o estimates that are similar to the values available in the literature related to snow avalanches and granular flows, where $C_o = 2$, $C_o = 1.5$–1.7, $C_o = 1.5$ are reported for rectangular, cylindrical and triangular geometries, respectively [19,96].

When we calculate the drag coefficients for the cold shear flows (/,/*) in Figs. 8 and 9 using Eq. (12), C_D falls within the 1.7–2.4 range. These values are consistent with $1.5 \leq C_D \leq 2$ suggested in the literature for "dry" avalanches [19]. However, for the gravitational flow regimes (|,|*) in Figs. 8 and 9 the calculated $7.6 \leq C_D \leq 40.0$ differ substantially from the suggested $3 \leq C_D \leq 6$ for "wet" avalanches [19]. The wide range and the high values of the calculated C_D compared to the values from the literature are in line with the discrepancy between the narrow range of C_D in the literature compared to field measurements showing that C_D may span over an order of magnitude [7,50]. This discrepancy probably ensues from the lack of understanding of the physical avalanche–obstacle interaction processes in the gravitational flow regimes.

We can indirectly assess the accuracy of the estimates of C_o, C_w and K by comparing the estimated factor $\zeta = C_o^2 C_w = C_o C_w K$ in the gravitational regime to measured values from avalanches with flow heights of up to 5.4 m and velocities of 1–8 m/s reported by Sovilla et al. [9]. For the comparison, we assume, based on the Vallée de la Sionne pylon's geometry (see Fig. 7), that the ζ values on the pylon must approximately correspond to the average of the estimated values of the cylindrical and triangular obstacles. For the factor C_w, we consider $w = 0.6$ m to be the relevant width, which corresponds to the width of the pylon [52]. In these configurations, we estimate $\zeta = 5.4$ for the cylindrical obstacle and $\zeta = 3.8$ for the triangular obstacle impacted by a cold plug flow (|). The lower bound of $\zeta = 4.6$ from the Vallée de la Sionne measurement data is consistent with the average of the estimated values. This consistency confirms that the estimation procedure yields reasonable results for the cold plug flow (|). Considering that the pressure increase induced by an increase in

cohesive bond strength in these specific avalanches from Sovilla et al. [9] may be of a factor of 2.0 to 2.5 [53], we estimate $\zeta = 7.6$ for the cylindrical obstacle and $\zeta = 13.5$ for the triangular obstacle. The upper bound of $\zeta = 10.4$ from measurements corresponds almost to mean value of the estimated ones. Hence, considering the uncertainty of the choice of the cohesive bond strength σ_{coh} and the potential dependency of f_{coh} on the geometry, the estimated values are remarkably close to the measured ones.

In order to assess the practical relevance of the proposed method to estimate C_D in real avalanche scenarios (|*,/*), we compare impact pressure calculations based on the C_D estimates to the pressure measured on the Vallée de la Sionne obstacles in Fig. 9. Although p_x is underestimated in two cases, due to a uncertain choice of C_w (see Section 7.2), considering the simplicity of the proposed method we can assert that the calculated pressure profiles show good agreement with the measured profiles. We show that by considering the gravitational and inertial contributions with the proposed method, we can calculate the vertical pressure distributions on the obstacle. As mentioned in Section 8.1, this may be of interest for the calculation of critical bending moments in inertial avalanches or high pressures at the flow base of gravitational avalanches.

9. Conclusions

In the present study, we have shown that our DEM simulations were able to reproduce how a snow avalanche impinges on obstacles of different geometries. Simulated and measured pressures showed good agreement. We simulated impact pressures on obstacles with rectangular, circular and triangular cross-sections in four typical avalanche flow scenarios, and we quantified how the impact pressure varied as a function of the obstacle geometry, width and avalanche flow regime. Furthermore, we documented how impact pressure was distributed on the obstacle surface for different geometries and flow regimes.

Based on previous studies on avalanche impact pressure – through field measurements [7,9,52,86] and DEM simulations [53,56] – and the new simulations presented in this paper, we have proposed a physics-based method for estimating the drag coefficient C_D involved in the definition of the impact pressure. An innovative point of our study is that the proposed calculation method can be applied to various obstacle geometries by using the specific geometry coefficient C_o.

An important outcome is that C_D varies continuously between the subcritical and supercritical regimes, and thus by using Eqs. (1) and (12) one can compute impact pressure with no assumption about the flow regime. When computing average impact pressures and vertical pressure profiles using the new method for estimating C_D, we obtained good qualitative agreement between impact pressure measurements and simulations for all flow regimes. On average, impact pressure can be predicted with a relative uncertainty lower than $\sim 20\%$.

Further work is needed to elucidate the physical processes underlying the dependence of impact pressure on obstacle width (through the C_w factor). The assumption $K = C_o$ is a coarse approximation based on an earlier study, where we showed that impact pressure depends on material compression inside the domain of influence around the obstacle [56]. Further improvements of our method could be achieved by calibrating the dependence of factor K on the flow regime, e.g., by conducting a study on the behavior of snow subjected to large compressive deformations. Moreover, in order to better account for the similarity between K and the earth pressure coefficient, the physical relevance of K could probably be further increased by adding a friction dependent term, e.g. similar to Jaky's solution [97]. Indeed, friction may be another important parameter which we did not analyze specifically in the current work. The role of friction and its implications on K could therefore be analyzed in detail in the future.

Code availability

The code that can be used with the Itasca PFC3D software to reproduce the data presented in this paper is available in the open access data repository Zenodo, which is financed by the Horizon 2020 project OpenAIRE and hosted by CERN. The associated entry can be accessed via Kyburz M., Sovilla, B., Gaume J., & Ancey C. (2021). Physics-based estimates of drag coefficients for the impact pressure calculation of dense snow avalanches. Zenodo. https://doi.org/10.5281/zenodo.4394455.

CRediT authorship contribution statement

M.L. Kyburz: Conceptualization, Methodology, Software, Formal analysis, Investigation, Visualization, Writing – original draft. **B. Sovilla:** Funding acquisition, Conceptualization, Experimental data curation & investigation, Writing – review & editing, Supervision. **J. Gaume:** Methodology, Writing - review & editing. **C. Ancey:** Writing - review & editing, Supervision.

Declaration of competing interest

The authors declare that they have no known competing financial interests or personal relationships that could have appeared to influence the work reported in this paper.

Availability of data and material

Further data and material is also available from: https://doi.org/10.5281/zenodo.4394455.

Acknowledgments

Michael L. Kyburz, Betty Sovilla and Christophe Ancey acknowledge the Swiss National Science Foundation for funding the project "Pressure on obstacles induced by granular snow avalanches" (grant no. 200021_169640). Johan Gaume acknowledges financial support from the Swiss National Science Foundation (grant no. PCEFP2_181227).

We acknowledge the efforts made by the editor Guenther Meschke, as well as Thierry Faug and another anonymous reviewer, for their constructive comments, which helped to improve the manuscript.

Funding

SNSF grant no. 200021_169640 and grant no. PCEFP2_181227.

Appendix A. Supplementary data

The supplementary material related to this article can be found online at https://doi.org/10.1016/j.engstruct.2021.113478 and contains details about the simulation procedure, the contact model and the calculation parameters for Sec. 7.2.

References

[1] Haefeli R. Schneemechanik mit hinweisen auf die erdbaumechanik. (Dissertation), Technischen Wissenschaften ETH Zürich, Nr. 997, ETHZ; 1939.
[2] Haefeli R. Neuere entwicklungstendenzen und probleme des lawinenverbaus im anbruchgebiet. Technical report, Buchdruckerei Büchler & Co; 1951.
[3] Ancey C, Bain V. Dynamics of glide avalanches and snow gliding. Rev Geophys 2015;53(3):745–84. http://dx.doi.org/10.1002/2015RG000491.
[4] Faug T. Macroscopic force experienced by extended objects in granular flows over a very broad Froude-number range. Eur Phys J E 2015;38(5):34. http://dx.doi.org/10.1140/epje/i2015-15034-3.
[5] Gauer P, Jóhannesson T. Loads on masts and narrow obstacles. Brussels; 2009, p. 95–108,
[6] Gauer P, Kristensen K. Four decades of observations from NGI's full-scale avalanche test site ryggfonn – Summary of experimental results. Cold Reg Sci & Technol 2016;125:162–76. http://dx.doi.org/10.1016/j.coldregions.2016.02.009.

[7] Thibert E, Faug T, Bellot H, Baroudi D. Avalanche impact pressure on a plate-like obstacle, in: International snow science workshop, Grenoble–Chamonix, France, 2013, pp. 663–667.

[8] Thibert E, Baroudi D, Limam A, Berthet-Rambaud P. Avalanche impact pressure on an instrumented structure. Cold Reg Sci & Technol 2008;54(3):206–15. http://dx.doi.org/10.1016/j.coldregions.2008.01.005.

[9] Sovilla B, Kern M, Schaer M. Slow drag in wet-snow avalanche flow. J Glaciol 2010;56(198):587–92. http://dx.doi.org/10.3189/002214310793146287.

[10] Haefeli R. Schnee, lawinen, firn und gletscher, in: Vienna, ISBN: 978-3-7091-5845-6, 1948, pp. 663–735, 10.1007/978-3-7091-5845-6_13.

[11] Perla R. Avalanche release, motion, and impact, in: 978-0-12-179450-7, 1980, pp. 397–462, 10.1016/B978-0-12-179450-7.50012-7.

[12] Hopfinger EJ. Snow avalanche motion and related phenomena. Annu Rev Fluid Mech 1983;15(1):47–76. http://dx.doi.org/10.1146/annurev.fl.15.010183.000403.

[13] Hutter K. Avalanche dynamics. In: Dordrecht. 1996, p. 317–92.

[14] Ancey C. Gravity flow on steep slope. Cambridge University Press; 2012, p. 372–432. http://dx.doi.org/10.1017/CBO9780511920196.011.

[15] White FM. Viscous fluid flow. New York: McGraw-Hill; 1991.

[16] Mellor M. Chapter 23 - dynamics of snow avalanches. In: Voight B, editor. Rockslides and avalanches, 1. Developments in geotechnical engineering, vol. 14, Elsevier; 1978, p. 753–92. http://dx.doi.org/10.1016/B978-0-444-41507-3.50031-3.

[17] Burkard A, Gubler HU, Salm BW. Berechnung von Fliesslawinen: eine Anleitung für Praktiker mit Beispielen. In: Mitteilungen des eidgenössischen instituts für schnee- und lawinenforschung, In: Mitteilungen des eidgenössischen instituts für schnee- und lawinenforschung, 1990.vol. 47.

[18] Mears A. Snow-avalanche hazard analysis for land-use planning and engineering. Technical report bulletin 49, Colorado Geological Survey; 1992.

[19] Jóhannesson Tómas, Gauer Peter, Issler P, Lied K. The design of avalanche protection dams: Recent practical and theoretical developments. European Commission - Directorate General for Research; 2009.

[20] de Quervain R. Avalanche atlas. Paris: Unesco; 1981.

[21] McClung D, Schaerer P. The avalanche handbook. The Mountaineers, Seattle; 1993.

[22] Coaz JWF. Die lauinen der schweizeralpen. J. Dalp'sche Buch- Und Kunsthandlung 1881. http://dx.doi.org/10.3931/e-rara-21209.

[23] Mougin P. Les avalanches en savoie. IV. Paris: MinistÈre de L'Agriculture, Direction Générale des Eaux et Forêts, Service des Grandes Forces Hydrauliques; 1922.

[24] Allix A. Les avalanches. Revue de GÉographie Alpine 1925;13:359–419.

[25] Paulcke W. Verständliche wissenschaft. In: Praktische schnee-und lawinenkunde. Springer-Verlag Berlin Heidelberg; 1938, p. 196–7. http://dx.doi.org/10.1007/978-3-642-99146-2.

[26] Ancey C. Snow avalanches. Oxford; 2016, http://dx.doi.org/10.1093/acrefore/9780199389407.013.17.

[27] Steinkogler W, Sovilla B, Lehning M. Influence of snow cover properties on avalanche dynamics. Cold Reg Sci & Technol 2014;97(Supplement C):121–31. http://dx.doi.org/10.1016/j.coldregions.2013.10.002.

[28] Steinkogler W, Gaume J, Löwe H. Sovilla B, Lehning M. Granulation of snow: From tumbler experiments to discrete element simulations. J Geophys Res Earth Surf 2015;120(6):1107–26. http://dx.doi.org/10.1002/2014JF003294.

[29] Köhler A. McElwaine J, Sovilla B. GEODAR Data and the flow regimes of snow avalanches. J Geophys Res Earth Surf 2018. http://dx.doi.org/10.1002/2017JF004375.

[30] Fischer J-T, Kaitna R, Heil K, Reiweger I. The heat of the flow: Thermal equilibrium in gravitational mass flows. Geophys Res Lett 2018;45(20). http://dx.doi.org/10.1029/2018GL079585, 11, 219–11, 226.

[31] Roch A. Mesure de la force des avalanches. In: Sonderdruck aus winterbericht 1960/61, Nr. 25. Schnee- und Lawinen Forschung; 1961.

[32] Brugnot G, Vila J-P. Investigation théorique et expérimentale des caractéristiques dynamiques des avalanches de neige dense. La Houille Blanche 1985;2:133–42.

[33] Sokratov S. The Russian contribution to snow science. Ice 2013;162:4–9.

[34] Zimmermann E. Von Lawinen. Schweizerische Bauzeitung 1936;107–108(25):541–3. http://dx.doi.org/10.5169/seals-48319.

[35] Voellmy A. Üer die Zerstörungskraft von Lawinen. IV. Zur lawinen-wirkung und ihrer bekämpfung. Schweizerische Bauzeitung 1955;73:280–5.

[36] Voellmy A. Üer die Zerstörungskraft von Lawinen. III. Stau- und Druckwirkungen. Schweizerische Bauzeitung 1955;73:246–9.

[37] Voellmy A. Üer die Zerstörungskraft von Lawinen. II. Zur Dynamik der Lawinen. Schweizerische Bauzeitung 1955;73:212–7.

[38] Voellmy A. Üer die Zerstörungskraft von Lawinen. Schweizerische Bauzeitung 1955;73:159–65.

[39] Salm B. On nonuniform, steady flow of avalanching snow. In: Assemblée générale de berne, publication No. 79. Berne: IAHS Wallingford Oxfordshire U.K.; 1967.

[40] Salm B. Contribution to avalanche dynamics. Scientific Aspects of Snow and Ice Avalanche 1966;69:199–214.

[41] Mellor M. Avalanches. In: Cold regions science and engineering. Part III: Engineering. Section A3: Snow technology. Hanover, New Hampshire: U.S. Army Material Command, Cold Regions Research & Engineering Laboratory; 1968.

[42] Bozhinskiy N, Losev K. The fundamentals of avalanche science. Technical report 55, EISFL; 1998.

[43] Rudolf-Miklau F, Sauermoser S, Mears A. (Eds.) F, Sauermoser S, Mears AI. The technical avalanche protection handbook. Berlin: Ernst & Sohn; 2014, http://dx.doi.org/10.1002/9783433603840.

[44] Margreth S, Stoffel L, Schaer M. BerÜCksichtigung der lawinen- und schneedruck-gefährdung bei seilbahnen. Ein leitfaden für die praxis. No. 28 in WSL Berichte. WSL-INstitut FÜR Schnee- Und Lawinenforschung SLF; Eidg, Forschungsanstalt für Wald, Schnee und Landschaft WSL; 2015.

[45] Roch A. Neve e valanghe. Torino: Club Alpino Italiano; 1980.

[46] Norem H. Estimating snow avalanche impact pressures on towers. In: Mitteilungen Nr. 48. Davos: Swiss Federal Institute for Snow and Avalanches; 1990, p. 42–56.

[47] Ancey C. Dynamique des avalanches. Lausanne: Presses Polytechniques et Universitaires Romandes; 2006.

[48] Issler D. European avalanche test sites: Overview and analysis in view of coordinated experiments. Technical report Mitteilungen Nr. 59, WSL/SLF; 1999.

[49] Gauer P, Issler D, Lied K, Kristensen K, Sandersen F. On snow avalanche flow regimes: Inferences from observations and measurements. In: International snow science workshop, Whistler; 2008. p. 717–23.

[50] Sovilla B, Schaer M, Kern M, P. Bartelt. Impact pressures and flow regimes in dense snow avalanches observed at the Vallée de la Sionne test site. J Geophys Res Earth Surf 2008a);113(F1). http://dx.doi.org/10.1029/2006JF000688.

[51] Baroudi D, Sovilla B, Thibert E. Effects of flow regime and sensor geometry on snow avalanche impact-pressure measurements. J Glaciol 2011;57(202):277–88. http://dx.doi.org/10.3189/002214311796405988.

[52] Sovilla B, Faug T, Köhler A. Baroudi D, Fischer J-T, Thibert E. Gravitational wet avalanche pressure on pylon-like structures. Cold Reg Sci & Technol 2016;126(Supplement C):66–75. http://dx.doi.org/10.1016/j.coldregions.2016.03.002.

[53] Kyburz M L, Sovilla B, Gaume J, Ancey C. Decoupling the role of inertia, friction, and cohesion in dense granular avalanche pressure build-up on obstacles. J Geophys Res Earth Surf 2020;125(2). http://dx.doi.org/10.1029/2019JF005192.

[54] Geng J, Behringer RP. Slow drag in two-dimensional granular media. Phys Rev E 2005;71:011302. http://dx.doi.org/10.1103/PhysRevE.71.011302.

[55] Chehata D, Zenit R, Wassgren CR. Dense granular flow around an immersed cylinder. Phys Fluids 2003;15(6):1622–31. http://dx.doi.org/10.1063/1.1571826.

[56] Kyburz M L, Sovilla B, Gaume J, Ancey C. The concept of the mobilized domain: how it can explain and predict the forces exerted by a cohesive granular avalanche on an obstacle. Granul Matter in press. http://dx.doi.org/10.1007/s10035-021-01196-1.

[57] Calvetti F, di Prisco CG, Vairaktaris E. DEM Assessment of impact forces of dry granular masses on rigid barriers. Acta Geotech 2017;12(1):129–44. http://dx.doi.org/10.1007/s11440-016-0434-z.

[58] Shen W, Zhao T, Zhao J, Dai F, Zhou GG. Quantifying the impact of dry debris flow against a rigid barrier by DEM analyses. Eng Geol 2018;241:86–96.

[59] Leonardi A, Goodwin G, Pirulli M. The force exerted by granular flows on slit dams. Acta Geotech 2019;14(6):1949–63. http://dx.doi.org/10.1007/s11440-019-00842-6.

[60] Scheiwiller T, Hutter K. Übersicht über experimente und theoretische modelle von fliess-und staublawinen. Technical report Mitteilung Nr. 58, VAW, ETH Zürich; 1982.

[61] Salm B, Gubler H. Measurement and analysis of the motion of dense flow avalanches. Ann Glaciol 1985;6:26–34. http://dx.doi.org/10.3189/1985AoG6-1-26-34.

[62] Cundall PA, Strack ODL. A discrete numerical model for granular assemblies. Géotechnique 1979;29(1):47–65. http://dx.doi.org/10.1680/geot.1979.29.1.47.

[63] Potyondy D, Cundall P. A bonded-particle model for rock. Int J Rock Mech Min Sci 2004;41(8):1329–64. http://dx.doi.org/10.1016/j.ijrmms.2004.09.011.

[64] Shapiro LH, Johnson J, Sturm M, Blaisdell G. Snow mechanics: Review of the state of knowledge and applications. CRREL Report 1997;97(3). 40.

[65] Scapozza C. Entwicklung eines dichte-und temperaturabhängigen stoffgesetzes zur beschreibung des visko-elastischen verhaltens Von Schnee. [Ph.D. thesis], ETH Zürich; 2004, http://dx.doi.org/10.3929/ethz-a-004680249.

[66] Salm B. Anlage zur untersuchung dynamischer wirkungen von bewegtem schnee. Zeitschrift FÜr Angewandte Mathematik Und Physik ZAMP 1964;15(4):357–75. http://dx.doi.org/10.1007/BF01601287.

[67] Rognon PG, Chevoir F, Bellot H, Ousset F, Naaim M, Coussot P. Rheology of dense snow flows: Inferences from steady state chute-flow experiments. J Rheol 2008a;52(3):729–48. http://dx.doi.org/10.1122/1.2897609.

[68] Kern M, Bartelt P, Sovilla B, Buser O. Measured shear rates in large dry and wet snow avalanches. J Glaciol 2009;55(190):327–38. http://dx.doi.org/10.3189/002214309788608714.

[69] Platzer K, Bartelt P, Kern M. Measurements of dense snow avalanche basal shear to normal stress ratios (S/N). Geophys Res Lett 2007;34(7). http://dx.doi.org/10.1029/2006GL028670, L07501.

[70] Bartelt P, McArdell BW. Granulometric investigations of snow avalanches. J Glaciol 2009;55(193):829–33. http://dx.doi.org/10.3189/002214309790152384.

[71] Issler D, Gauer P, Schaer M, Keller S. Inferences on mixed snow avalanches from field observations. Geosciences 2020;10(1). http://dx.doi.org/10.3390/geosciences10010002.
[72] Bucher E, Roch A. Reibungs- und packungswiederstäe bei raschen schneebewegungen. Technical report 31, SLF; 1946.
[73] Kuroiwa D, Mizuno Y, Takeuchi M. Micromeritical properties of snow. Phys Snow Ice Proc 1967;1(2):751–72.
[74] Yong R, Fukue M. Performance of snow in confined compression. J Terramech 1977;14(2):59–82. http://dx.doi.org/10.1016/0022-4898(77)90002-7.
[75] Gerling B, Löwe H. van Herwijnen A. Measuring the elastic modulus of snow. Geophys Res Lett 2017;44(21):11, 088–96. http://dx.doi.org/10.1002/2017GL075110.
[76] Ammann WJ. A new swiss test-site for avalanche experiments in the Vallée de la Sionne/Valais. Cold Reg Sci & Technol 1999;30(1):3–11. http://dx.doi.org/10.1016/S0165-232X(99)00010-5.
[77] Sovilla B, Margreth S, Schaer M, Ancey C. Taking into account wet avalanche load for the design of pylon-like structures. In: International snow science workshop, Banff, Canada; 2014. p. 727–32.
[78] Kern MA, Bartelt PA, Sovilla B. Velocity profile inversion in dense avalanche flow. Ann Glaciol 2010;51(54):27–31. http://dx.doi.org/10.3189/172756410791386643.
[79] Rognon PG, Roux J-N, Naaim M, Chevoir F. Dense flows of cohesive granular materials. J Fluid Mech 2008b;596:21–47. http://dx.doi.org/10.1017/S0022112007009329.
[80] Rognon PG, Roux J-N, Wolf D, Naaim M, Chevoir F. Rheophysics of cohesive granular materials. Europhys Lett (EPL) 2006;74(4):644–50. http://dx.doi.org/10.1209/epl/i2005-10578-y.
[81] Issler D. Experimental information on the dynamics of dry-snow avalanches. Berlin, Heidelberg: Springer Berlin Heidelberg; 2003, p. 109–60. http://dx.doi.org/10.1007/978-3-540-36565-5_4.
[82] McClung D, Schaerer PA. The avalanche handbook. The Mountaineers Books; 2006.
[83] Wieghardt K. Experiments in granular flow. Annu Rev Fluid Mech 1975;7(1):89–114. http://dx.doi.org/10.1146/annurev.fl.07.010175.000513.
[84] Albert R, Pfeifer M, Barabasi A-L, Schiffer P. Slow drag in a granular medium. Phys Rev Lett 1999;82:205–8. http://dx.doi.org/10.1103/PhysRevLett.82.205.
[85] Faug T. Granular force on objects and correlation length: Drag coefficient enhancement in low Froude number flow regimes. AIP Conf Proc 2013;1542(1):617–21. http://dx.doi.org/10.1063/1.4812007.
[86] Thibert E, Bellot H, Ravanat X, Ousset F, Pulfer G, Naaim M, Hagenmuller P, Naaim-Bouvet F, Faug T, Nishimura K, Ito Y, Baroudi D, Prokop A, Schön P. Soruco A, Vincent C, Limam A, Héno R. The full-scale avalanche test-site at Lautaret Pass (French Alps). Cold Reg Sci & Technol 2015;115:30–41. http://dx.doi.org/10.1016/j.coldregions.2015.03.005.
[87] Favier L, Daudon D, Donzé F-V. Rigid obstacle impacted by a supercritical cohesive granular flow using a 3D discrete element model. Cold Reg Sci & Technol 2013;85:232–41. http://dx.doi.org/10.1016/j.coldregions.2012.09.010.
[88] Roy S, Luding S, Weinhart T. A general(ized) local rheology for wet granular materials. New J Phys 2017;19(4):043014. http://dx.doi.org/10.1088/1367-2630/aa6141.
[89] McClung DM, Schaerer PA. Characteristics of flowing snow and avalanche impact pressures. Ann Glaciol 1985;6:9–14. http://dx.doi.org/10.3189/1985AoG6-1-9-14.
[90] Silbert LE, Landry JW, Grest GS. Granular flow down a rough inclined plane: Transition between thin and thick piles. Phys Fluids 2003;15(1):1–10. http://dx.doi.org/10.1063/1.1521719.
[91] Kern M, Tiefenbacher F, McElwaine J. The rheology of snow in large chute flows. Cold Reg Sci & Technol 2004;39(2):181–92. http://dx.doi.org/10.1016/j.coldregions.2004.03.006.
[92] Huang D, Lee JH. Mechanical properties of snow using indentation tests: size effects. J Glaciol 2013;59(213):35–46. http://dx.doi.org/10.3189/2013JoG12J064.
[93] Gubler H, Hiller M, Klausegger G, Suter U. Messungen an fliesslawinen. SLF; 1986.
[94] Faug T, Turnbull B, Gauer P. Looking beyond the powder/dense flow avalanche dichotomy. J Geophys Res Earth Surf 2018;123(6):1183–6. http://dx.doi.org/10.1002/2018JF004665.
[95] Armanini A. On the dynamic impact of debris flows. In: Lecture notes in earth sciences, vol. 64, Berlin: Springer; 1997, p. 208–26.
[96] Favier L, Daudon D, Donzé F, Mazars J. Discrete element modelling to compute drag coefficients of obstacles impacted by granular flows. In: International snow science workshop, Davos, Switzerland; 2009. p. 500–4.
[97] Jaky J. The coefficient of earth pressure at rest. J Soc Hungarian Archit Eng 1944;355–8.